

Reduced-model scrape-off layer turbulence (nSOLT)
simulations comparing three fueling scenarios:
pellet injection (core), divertor recycling (edge), and
neutral puffing (SOL)

D.A. Russell and J.R. Myra

Lodestar Research Corporation, Boulder, Colorado 80301, USA

F. Militello and D. Moulton

CCFE, Culham Science Centre, Abingdon, Oxon OX14 3DB, United Kingdom

July 2021

prepared for submission to the
Physics of Plasmas

ER/54392-98

LRC-21-188

LODESTAR RESEARCH CORPORATION
5055 Chaparral Court, Suite 102
Boulder, Colorado 80301

Reduced-model scrape-off layer turbulence (nSOLT) simulations comparing three fueling scenarios: pellet injection (core), divertor recycling (edge), and neutral puffing (SOL)

D.A. Russell and J.R. Myra
Lodestar Research Corporation, Boulder, CO 80301, USA

F. Militello and D. Moulton
CCFE, Culham Science Centre, Abingdon, Oxon OX14 3DB, United Kingdom

Abstract

The 2D scrape-off-layer turbulence code (nSOLT) includes 1D Boltzmann neutral-plasma interactions, a model of divertor recycling (introduced here), and a fixed source of plasma concentrated at the core-side boundary. 1) Neutral injection in the far-SOL is accomplished by specifying the density of Franck-Condon distributed neutrals streaming in from the boundary. 2) Divertor recycling is modeled by injecting a fraction of the particle parallel flux in the SOL back into the edge region as a source of plasma. 3) A constant source fuels the edge plasma from the core-side boundary to model pellet injection. For machine parameters (B , R_m , $L_{//}$) illustrative of the MAST-U device, and for a deuterium plasma, turbulent equilibria are obtained that share the *same plasma fueling rate* for each of the three fueling methods, with only one of the sources on in each case. In the presence of self-consistent turbulence, quasi-steady plasma and neutral (deuterium) profiles, fueling efficiencies, SOL transparencies, and heat flux widths are compared. Characteristics of the turbulent fluctuations, including skewness, cross-phases and power spectra, are described. The calculated fueling efficiencies, SOL transparencies and many of the turbulent properties are remarkably similar for all three fueling methods despite significant differences in the plasma profiles. The nonlinear states of the three cases are dominated by separatrix-spanning vortex cells that control particle and heat losses into the SOL.

I. Introduction

Fueling impacts the distribution of plasma density and temperature and consequently the character of turbulent fluctuations and transport in the edge and SOL regions of the tokamak. Results of experiments on DIII-D demonstrate that high-confinement mode (H-mode) accessibility and tolerable heat-flux loading at the divertor, both crucial for ITER operation, depend critically on the fueling scenario. [1]

Fueling scenarios can be distinguished by the efficiency with which they add plasma to the core and edge regions of the tokamak. *Pellet fueling* creates plasma directly in the core region by ionization of an injected ice pellet of the hydrogenic fuel; the new plasma spreads radially outward into the edge and scrape-off layer (SOL) regions. Neutral beam injection (NBI) and supersonic molecular beam injection (SMBI) similarly supply sources concentrated in the core region. *Puff fueling*, on the other hand, injects neutral gas molecules (D_2) through ports in the machine wall which dissociate and stream across the SOL as atoms that are ionized in the higher-temperature environment of the near-SOL and edge regions. An internally self-consistent

cousin of puff injection is *divertor recycling*: Plasma bombardment of material surfaces causes recycling of neutrals that are ionized once they reach the edge region and proceed from there to fuel the core.

Numerical simulation codes used to describe neutral-plasma interactions in the tokamak range from the gyrokinetic PIC codes, exemplified by XGC1 [2] to the diffusive transport codes, exemplified by UEDGE [3] and SOLPS-ITER [4]. PIC codes model fluctuations on the scale of the ion gyro-radius but are relatively expensive to run, particularly when used to simulate an entire section of the tokamak on long time scales. Transport codes do not evolve plasma turbulent fluctuations but instead use ad hoc diffusion coefficients to model plasma transport. Plasma fluid simulation codes are less expensive than PIC codes to run but, unlike transport codes, resolve turbulent fluctuations in the collisional plasma regime. For example, the BOUT++ code [5] and models based on the BOUT++ framework [6] are based on the Braginskii fluid model equations. [7]

Among the fluid codes, the plasma evolution may be coupled *either* to a fluid description of the neutral species evolution, appropriate in the small neutral mean-free-path limit, exemplified by the BOUT++ framework with *trans-neut* module [8], the models of Bisai et al. [9, 10, 11] and by the nHESSEL code of Thrysøe et al., [12, 13] *or* to a kinetic (Boltzmann) description of that evolution, as in the GBS code of Wersal and Ricci [14, 15] and in the nSOLT code [16] used in the present study. nSOLT is perhaps closest to GBS but is much reduced in focus. Where GBS models the entire tokamak in three dimensions, nSOLT simulates plasma turbulence in two dimensions in the outboard midplane region of the tokamak, including the edge and SOL, and uses a unique parallel transport model on the open field lines to achieve that reduction. nSOLT is arguably the most reduced of the fluid-plasma, kinetic-neutrals turbulence simulation codes. A brief roundup of currently active modeling is given in reference [16].

We present results of nSOLT simulations of plasma turbulence driven by three distinct fueling methods: pellet injection, divertor recycling and neutral puff injection. Recent numerical studies that have specifically addressed issues of fueling include: the work of Zhou et al. [17] who used the BOUT++ framework to simulate gas puffing and SMBI in the vicinity of the HL-2A tokamak divertor; the transport model-based studies of Koechl et al., [18] and those of Polevoi et al. [19] that explored efficiency issues for ITER fueling by gas puffing and/or pellet injection; the work of Koikea et al. [20] that explored fueling by the merging of two co-axial plasma rings; and the NSTX-U fueling studies using UEDGE and DEGAS 2 simulations (diffusive plasma transport coupled to kinetic Monte-Carlo neutral species evolution) by Scotti et al. [21]

To the best of our knowledge, this is the first comparative study of fueling scenarios that uses a reduced fluid-plasma description of turbulent evolution coupled to a kinetic description of the neutral atomic component.

The remainder of the paper is organized as follows. Section II presents the nSOLT model equations of evolution. Section III describes the modelling of the three plasma sources. Section IV introduces our definitions of SOL transparency and fueling efficiency. Parallel energy flux,

heat flux widths and the power budget in the SOL are discussed in Sec. V. The turbulent fluctuations are diagnosed in Sec. VI. A summary and concluding remarks are given in Sec. VII. Appendix A gives explicit expressions for the parallel fluxes on open and closed field lines, and Appendix B gives details of the power budget calculation in the SOL.

II. Model equations

a. Overview

The nSOLT model [16] describes the fluid plasma coupled to kinetic neutrals; it consists of four fluid equations of evolution for the plasma density (n_e), the electron and ion temperatures (T_e and T_i) and the ion fluid vorticity ($-\rho$) that are coupled to the evolution of the neutral atoms by a Boltzmann equation. The plasma equations are reduced from the more general drift-ordered reduced Braginskii fluid model derived by Simakov and Catto [22] by making assumptions appropriate to the outboard midplane (OM) region of a tokamak. These assumptions plus “closure relations” [23] reduce the plasma simulation domain to two spatial dimensions (2D). The “bi-directional” (approximately poloidal) variable (y) is in the dimension perpendicular to the B-field and to the radial dimension (x). The Boltzmann equation evolves the y -averaged neutral distribution function, $G(x, v_x, t)$, in the radial dimension. Only the y -averages of plasma fields appear in the evolution of G , and the plasma sees neutrals that are homogeneously distributed in y . Although the fundamental neutral-plasma interactions in the model remain valid in the short mean free path limit, this description is most appropriate for the neutrals in the long mean-free-path regime because in that case the neutrals average over plasma conditions in the y direction.

With the magnetic (B) field in the z -direction, the simulation plane (x, y) includes closed field lines in the edge region ($\Delta x < 0$) and open field lines in the scrape-off-layer (SOL) region ($\Delta x > 0$), where $\Delta x = x - x_{\text{sep}}$, and x_{sep} locates the magnetic separatrix. It is assumed that (1) the parallel gradients of even velocity moments of the distribution functions (i.e., $\nabla_{\parallel} n_{e,i}$, $\nabla_{\parallel} T_{e,i}$, $\nabla_{\parallel} P_{e,i}$) vanish in both the edge and SOL regions at the OM, and that (2) parallel fluxes in the SOL (i.e., odd moments of the distribution functions) are odd about the simulation plane ($z=0$).

Assumption (1) expresses the observation that turbulent transport across the B-field is concentrated in a neighborhood of the OM where the interchange instability growth rate is maximized and that the plasma spreads out along the B-field away from this turbulent region. Assumption (2) says that the plasma drains away from the OM symmetrically along open field lines in the SOL toward the divertor(s). These assumptions are appropriate to the baseline double-null operating scenario in the MAST-U device.

Flux-surface (y) averages of parallel gradients must vanish in the edge region by periodicity (for $B \cong \text{constant}$), and they are constrained to do so by explicitly writing parallel gradients in the edge region as fluctuations with respect to y . In the SOL, “closure relations” [23] result from replacing parallel flux gradients, such as that of the current density, $\nabla_{\parallel} j_{\parallel}$, with their field-line averages taken from the OM ($z=0$) to $z=L_{\parallel}$. Exploiting assumption (2) this

average, viz., $[j_{\parallel}(z=L_{\parallel})-j_{\parallel}(z=0)]/L_{\parallel}$, is $j_{\parallel}(z=L_{\parallel})/L_{\parallel}$ where $L_{\parallel} = L_{\parallel}(x)$ is the parallel connection length to the divertor sheath, and $j_{\parallel}(z=L_{\parallel})$ is the parallel current at the divertor sheath entrance. The closure relations effectively map sheath boundary conditions into the OM. Disconnection from the sheath resulting from volume resistivity (conduction limited regime) is modeled heuristically. [23]

Convection is by the $\mathbf{E} \times \mathbf{B}$ velocity, $\mathbf{v}_E = \mathbf{b} \times \nabla \phi$, in a constant, uniform magnetic field $\mathbf{B} = b\mathbf{B}$ directed out of the (x,y) plane. Our model considers only electrostatic fluctuations, where ϕ is the electrostatic potential, and we ignore polarization drifts as negligible in comparison with \mathbf{v}_E , except in deriving the vorticity equation where the divergence of the polarization current is essential. [22]

The equations given below are in dimensionless (Bohm) units: time is measured in units of the ion gyro period (Ω_{ci}^{-1}), energies ($e\phi$, T_e , T_i) in units of a reference temperature (T_r), velocities in units of the corresponding cold ion acoustic speed ($c_{sr} = [T_r/m_i]^{1/2}$), length in units of the reference ion gyro-radius (ρ_{sr}) based on the sound speed ($\rho_{sr} = c_{sr}\Omega_{ci}^{-1}$), and density is in units of a reference density (n_r). We adopt fundamental parameters illustrative of a deuterium plasma at MAST-U: $B = 5745$ Gauss in the OM ($\Omega_{ci} = 2.75 \times 10^7$ rad/sec), OM machine radius $R_{0+} \equiv R_m = 132$ cm, and connection length profile $L_{\parallel}(x)$ as determined by field-line tracing from a magnetic equilibrium reconstruction. [24] These parameters result in the reference values $c_{sr} = 69$ km/sec and $\rho_{sr} = 2.52$ mm for the simulations of this paper, where $T_r = 100$ eV.

b. plasma density

The equation of evolution of the plasma density ($n = n_e = n_i$) is

$$\partial_t n + \nabla_{\perp} \cdot (\mathbf{v}_E n) = \nabla_{\perp} \cdot (\mathbf{D}_n \nabla_{\perp} n) - \nabla_{\parallel} \Gamma_{\parallel e} + \mathbf{S}_P + \mathbf{S}_D + \mathbf{S}_{IZ}, \quad (1)$$

where $\nabla_{\perp} = e_x \partial_x + e_y \partial_y$. The diffusion coefficient D_n is unphysically large in a buffer zone that includes the simulation boundary in the edge region, or the ‘‘core-side’’ boundary, in order to suppress fluctuations that would otherwise cascade into large cells there, and to provide a controlled diffusive flux of pellet-injected plasma at that boundary (by the source \mathbf{S}_P) into the edge region. See Fig. 1. Outside of the buffer zone, D_n is a physically reasonable constant, given below. The parallel flux gradient, $\nabla_{\parallel} \Gamma_{\parallel e} = \nabla_{\parallel} (n_e v_{\parallel e})$, is given explicitly in Appendix A.

We consider three different particle sources in Eq. (1): \mathbf{S}_P represents a stationary source concentrated at the core-side boundary intended to model pellet injection. \mathbf{S}_D represents a source of plasma from recycling at the divertor and is concentrated in the edge region. \mathbf{S}_{IZ} is a source due to ionization of the neutral atoms puffed in from the far-SOL boundary. The sources are described further in Sec. III.

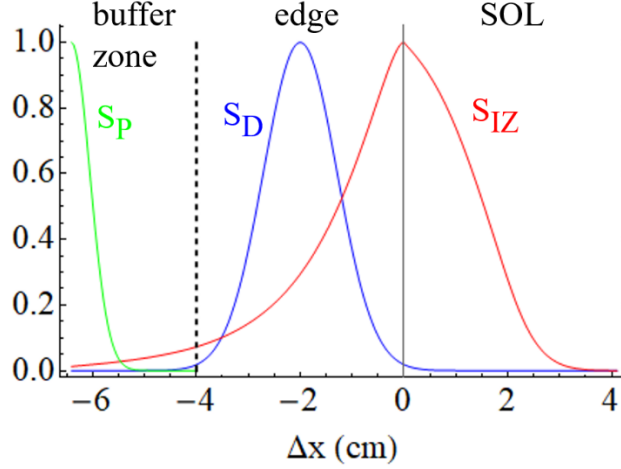


Fig. 1. The spatial distributions of the plasma sources modelled in the three simulations are plotted as functions of distance from the separatrix (Δx). Each has been renormalized to have a maximum value of one. S_P denotes the pellet source; S_D denotes the divertor-recycling source, and S_{IZ} is the source from ionization of “puffed” neutrals injected at the far-SOL boundary. The shapes of S_P and S_D are stationary; the time-average of S_{IZ} for the puffed case is shown. [Associated dataset available at <https://doi.org/10.5281/zenodo.4994177>]

c. plasma pressure

The electron and ion pressure evolution equations are, respectively,

$$\left[\partial_t \frac{3n}{2} T_e + \nabla_{\perp} \cdot (v_E \frac{3n}{2} T_e) \right] = \frac{3}{2} T_e S_D + \frac{3}{2} S_{Ee} + \nabla_{\perp} \cdot (\chi_e n \nabla_{\perp} T_e) - \langle \sigma v \rangle_{iz} n_0 n E_{iz} - \nabla_{\parallel} Q_{\parallel e} \quad (2a)$$

and

$$\left[\partial_t \frac{3n}{2} T_i + \nabla_{\perp} \cdot (v_E \frac{3n}{2} T_i) \right] = \frac{3}{2} T_i S_D + \frac{3}{2} S_{Ei} + \nabla_{\perp} \cdot (\chi_i n \nabla_{\perp} T_i) + (\langle \sigma v \rangle_{iz} + \langle \sigma v \rangle_{cx}) n_0 n E_0 - \frac{3}{2} \langle \sigma v \rangle_{cx} n_0 n T_i - \nabla_{\parallel} Q_{\parallel i} \quad (2b)$$

where the charge-exchange (CX) and ionization (IZ) rates, $n_0 \langle \sigma v \rangle_{cx}$ and $n_0 \langle \sigma v \rangle_{iz}$, describe energy exchange with the neutral population and are given below in Eqs. (4c) and (4d). n_0 and $n_0 E_0$ are the neutral particle and energy density moments of the distribution function G . In (2a) E_{iz} is the “ionization cost” responsible for cooling the electrons in the presence of neutrals. The plasma is heated by stationary sources, $S_{Ee,i}$, isolated within the buffer zone at the core-side boundary, but notice that the divertor recycling source S_D acts to heat the plasma in the OM edge

region as well. The pellet source, S_p , does not appear in these equations but is explicit in the equations for *temperature* evolution obtained by using Eq. (1) to eliminate $\partial_t n$ from (2a) and (2b). As for D_n , so the thermal diffusivities, $\chi_{e,i}$, are unphysically large in the buffer zone to provide a controlled diffusive flux of energy injected at that boundary by the sources $S_{Ee,i}$ into the edge region. See Fig. 1. Outside the buffer zone, χ_e and χ_i are physically defensible constants, given in Sec. III below. The parallel energy flux gradients $\nabla_{\parallel} Q_{|e,i}$ are given in Appendix A.

d. vorticity and electrostatic potential

The total ion fluid momentum density is $\mathbf{g} = n\mathbf{u} = n(\mathbf{v}_E + \mathbf{v}_{di})$, and the component of its curl, i.e., the vorticity, along \mathbf{b} is

$$n\nabla_{\perp}^2\phi + \nabla_{\perp}n \cdot \nabla_{\perp}\phi + \nabla_{\perp}^2 p_i = \mathbf{b} \cdot \nabla \times \mathbf{g} \equiv -\rho. \quad (3a)$$

[We define this vorticity to be $-\rho$ so that, in the cold-ion ($T_i=0$) and Boussinesq ($\nabla n=0$) approximations, ρ has the same sign as the charge density.] Given n , $p_i = nT_i$ and ρ , Eq. (3a) is solved for the electrostatic potential (ϕ) at each time step.

The evolution of ρ is as follows.

$$\begin{aligned} d_t \rho = & -2\mathbf{b} \times \boldsymbol{\kappa} \cdot \nabla(P_e + P_i) - (\partial_x f_y - \partial_y f_x) - \nabla_{\parallel} j_{\parallel} + \mu \nabla_{\perp}^2 \rho \\ & + \frac{1}{2} \left[n_e v_{di} \cdot \nabla_{\perp} \nabla_{\perp}^2 \phi \right] - \frac{1}{2} \left[v_E \cdot \nabla_{\perp} (\nabla_{\perp}^2 P_i) - \nabla_{\perp}^2 (v_E \cdot \nabla_{\perp} P_i) \right] - \frac{1}{2} \mathbf{b} \times \nabla n_e \cdot \nabla v_E^2 \end{aligned} \quad (3b)$$

where $\boldsymbol{\kappa} = \mathbf{b} \cdot \nabla \mathbf{b} = -\mathbf{e}_x \rho_{sr} / R_m$ is the curvature vector, μ is the coefficient of viscosity, \mathbf{f} is the neutral friction force density,

$$\mathbf{f} = \langle \sigma v \rangle_{iz} n_0 n_e \mathbf{v}_0 + \langle \sigma v \rangle_{cx} n_0 n_i (\mathbf{v}_0 - \mathbf{v}_E - \mathbf{v}_{di}), \quad (3c)$$

and \mathbf{v}_0 is the neutral fluid velocity. The radial (x) component of the neutral velocity is given by the v_x -moment of the neutral distribution function, G , while the evolution of the bi-directional component (v_{0y}) is given in (4b) below. The parallel current gradient, $\nabla_{\parallel} j_{\parallel}$, is given in Appendix A.

e. neutral distribution function

The evolution of the neutral species is described by the following equations.

$$\partial_t G + v_x \partial_x G = \langle \sigma v \rangle_{cx} n_0 F_i - \langle \sigma v \rangle_{cx} \bar{n}_i G - \langle \sigma v \rangle_{iz} \bar{n}_e G \quad (4a)$$

$$\partial_t v_{0y} + v_{0x} \partial_x v_{0y} = \langle \sigma v \rangle_{cx} \bar{n}_i (\bar{v}_{Ey} + \bar{v}_{diy} - v_{0y}) \quad (4b)$$

Here $G = G(t, x, v_x)$ is the 1D neutral species distribution function, and $F_i = F_i(t, x, v_x)$ is a 1D Maxwellian distribution function based on the y -averaged ion density and temperature,

$$F_i = \bar{n}_i \exp\left[-v_x^2 / (2\bar{T}_i)\right] / (2\pi\bar{T}_i)^{1/2}.$$

Only the y-averages of plasma fields, denoted by overbars, appear in the evolution of G, and the plasma sees neutrals that are homogeneously distributed in y. If the 3D neutral distribution function is denoted by g, then $G(x, v_x, t) = \int dv_y dv_z \bar{g}$, and we have assumed no toroidal (z) dependence. In Eqs. (4), $n_e = n_i \equiv n$; the distinction is purely to elucidate the underlying physical processes.

The form of the convective derivative in (4b) involves a closure ansatz for the $v_x v_y$ -moment of \bar{g} . We indicate the result of that ansatz and the evolution of G, derived from the Boltzmann equation for g, here and refer the reader to reference [16] for the derivations.

The charge exchange and ionization rates are similarly based on y-averaged electron and ion temperatures:

$$\langle \sigma v \rangle_{cx}(\bar{T}_i) = 1.1 \times 10^{-14} \bar{T}_i(x, t)^{0.3} M_i^{-1/2} \text{ m}^3/\text{sec} \quad \text{and} \quad (4c)$$

$$\langle \sigma v \rangle_{iz}(\bar{T}_e) = 8 \times 10^{-15} \bar{T}_e(x, t)^{1/2} \exp\left[-13.56 / \bar{T}_e(x, t)\right] / (1 + 0.01 \bar{T}_e(x, t)) \text{ m}^3 / \text{sec} \quad (4d)$$

where the temperatures are expressed in eV and M_i in AMU ($M_i = 2$ for D). These formulaic rates are fits to tabulated values of the collision rates that are used in kinetic neutral Monte Carlo simulations. [25]

f. boundary conditions

All plasma fields (n , T_e , T_i , ϕ) are periodic in y. The fluctuations in these fields (e.g., $\delta n = n - \bar{n}$, where the over-bar indicates the poloidal average or “mean” value) vanish at both x-boundaries of the domain $0 \leq x \leq L_x$. The mean values of the density and temperatures are held to constant “floor” values at the far-SOL boundary, and their radial gradients are held to zero at the core-side boundary so that there is no diffusive flux of those quantities at that boundary. The radial gradient of the mean potential ($\partial_x \bar{\phi} = \bar{v}_{Ey}$) is taken to be zero at the core-side boundary ($x=0$), and the mean potential is set equal to the Bohm potential at the SOL boundary, $\bar{\phi}(x = L_x, t) = 3\bar{T}_e(x = L_x, t)$, and these boundary conditions are used to solve Eq. (3a) for the potential.

At the far-SOL boundary ($x = L_x$), or “wall,” the boundary condition on G is given by

$$G(x=L_x, v_x < 0) = n_{\text{puff}} \exp[-(v_x - v_{D_2})^2 / 2T_{FC}] / (2\pi T_{FC})^{1/2} \quad (5)$$

where v_{D_2} is taken to be -0.8 km/sec, corresponding to room temperature (300° K) D_2 molecules, and T_{FC} is the Franck-Condon (FC) temperature, taken to be 3 eV. (This is a stationary fueling source; we do not consider the time-dependent recycling of neutrals and ions that impact the ‘main chamber’ wall.) Neutrals free-stream out of the simulation domain at both boundaries; exiting neutrals at the core-side boundary, $G(x=0, v<0)$, and at the wall, $G(x=L_x, v>0)$, are evolved by convection alone. No neutrals enter from the core: $G(x=0, v>0) = 0$. G is held to zero at the boundary of the velocity domain which extends to $(\pm) 4c_s$ (280 km/sec) and contains the observed support of G in the simulations.

g. Numerical methods

The overall updating of the plasma fields in nSOLT (n, T_e, T_i, ρ) is split-step: to each monomial term in the evolution equations there corresponds a subroutine that solves an initial value problem starting from the fields updated by the previous subroutine in the calling sequence of the main time loop. The algorithm used in the convection subroutine is flux-corrected transport (FCT) [26], chosen for its exceptional ability to resolve steep propagating fronts, e.g., density blobs. The alternating-direction implicit (ADI) algorithm [27] is used to advance the fields by linear diffusion [i.e., terms proportional to $D_n, \chi_{e,i}$ and μ in Eqs. (1), (2a, b) and (3b)]. The fields are updated explicitly by the parallel flux gradients ($\nabla_{\parallel} \Gamma_{\parallel e}, \nabla_{\parallel} Q_{\parallel e}, \nabla_{\parallel} Q_{\parallel i}, \nabla_{\parallel} j_{\parallel}$) and by the sources ($S_P, S_D, S_{IZ}, S_{Ee}, S_{Ei}$). The electrostatic potential (ϕ) is found by solving Eq. (3a) by the relaxation method of Angus and Umansky. [28]

The evolution of the neutral distribution function (G) is in three steps: free-streaming by upwind linear interpolation, CX update by a 2nd order Runge-Kutta method and an explicit exponential update for ionization. (The plasma fields are taken as fixed over a single time step, Δt .) The free-streaming update is constrained by $\max(|v_x|) \Delta t / \Delta x < 1$, where here v_x is the independent velocity variable of the neutral grid (x, v_x). With $\max(|v_x|) \sim c_s$ and $\Delta x \sim \rho_s$, this constraint amounts to $\Delta t < \Omega_i^{-1}$ which imposes no greater computational burden than that imposed by resolving the turbulent fluctuations, where $\Delta t \sim 10^{-2} \Omega_i^{-1}$ is typical in practice.

III. 3 plasma sources, synchronized

The plasma is fueled by one and only one of three sources that model pellet injection from the core-side boundary (S_P), divertor recycling in the edge region (S_D) and ionization of neutrals puffed into the simulation domain from the SOL boundary (S_{IZ}). See Eq. (1) and Fig. 1. (A weak puff is retained to provide diagnostics in the pellet and divertor-fueled cases but contributes negligibly to fueling.)

1) **Pellet fueling** is modeled by a stationary source, $S_P(x)$, concentrated in the buffer zone at the core-side boundary. Diffusion coefficients, that are much larger in the buffer zone than in the edge and SOL, exclude turbulent fluctuations while transporting pellet-injected plasma into the edge region by means of the diffusive flux $D_n \cdot \nabla n$.

2) **Divertor recycling** is modelled by injecting a fraction (R_D) of the parallel plasma flux ($\Gamma_{\parallel e}$) in the SOL back into the edge region. This recycling is instantaneous in our model; plasma is injected into the edge as soon as it leaves the SOL. The recycled plasma is introduced at the local edge temperature, under the assumption that the original divertor-emitted neutrals equilibrate by charge-exchange with the local plasma while in transit to the edge where they are ionized and then make their way to the OM. The source is

$$S_D(x, t) = R_D h(x) \int_{x_{SEP}}^{L_x} d\xi \langle \nabla_{\parallel} \Gamma_{\parallel e} \rangle_y(\xi, t), \quad (6)$$

where the profile $h(x)$ is a Gaussian centered in the edge and normalized to unity on the simulation domain, $\int_0^{L_x} dx h(x) = 1$. It can be seen from Eq. (1) that, with zero diffusive and turbulent radial flux at the boundaries, the integral of the y-averaged plasma density is conserved if $R_D = 1$: $\int_0^{L_x} dx \partial_t \bar{n}(x, t) = 0$. This fact is useful for adjusting the operating density in a turbulence simulation; the density is driven up rapidly with strong pellet injection or puffing that is switched off once a target density is reached. Continuing with $R_D = 1$ will maintain the density or, if the target is exceeded, temporarily switching to $R_D < 1$ will lower the density.

3) **Puff fueling** is by means of the far-SOL boundary condition on the neutral distribution function given in Eq. (5), Sec. III. From the wall, neutrals stream into the SOL and are ionized with increasing probability as they approach the edge, and the plasma that they encounter grows hotter and denser. The plasma density source from ionization is [See Eq. (1)]

$$S_{IZ}(x, y, t) = \langle \sigma v \rangle_{iz} n_0 n. \quad (7)$$

In the divertor-recycling (D) and pellet-fueled (P) simulations, a small puff (10^9cm^{-3}) provides a diagnostic of SOL transparency to neutral propagation but is a negligible fueling source in those cases.

Results from three nSOLT simulations are presented in the remainder of this paper that use each of the three fueling methods, respectively. The simulations have heating rates and diffusion coefficients in common: $S_{Ee,i}$ (maximum) = 30 MW/m³, $D_n = 0.2 \text{ m}^2/\text{sec}$, $\chi_{e,i} = 15 \text{ m}^2/\text{sec}$, and $\mu = 30 \text{ m}^2/\text{sec}$. The values given here for the diffusion coefficients, D_n and $\chi_{e,i}$, are for the edge and SOL, i.e., outside the buffer zone, and their values are taken from a reference SOLPS [4] simulation of an H-mode plasma at MAST-U. [24]

The source parameters were adjusted to bring the mean values of the respective core fueling rates (F) into agreement within standard deviations:

$$F = \int_{\Delta x < 0} dx (S_P, S_D, S_{IZ}). \quad (8)$$

First, by tuning the operating density of the divertor-recycling fueled simulation (D), as described above, it was possible to bring the equilibrium profiles into reasonable agreement with those of the reference SOLPS simulation in the SOL. That equilibrium set the target fueling rate for the other two simulations, trivial to reach in the pellet-fueled case by choosing the constant parameters of S_P to give the required integral in Eq. (8) but more challenging to reach in the puffed case due to the unpredictable dependence of the source on the condition of the plasma. At the time origin in Fig. 2 ($\Delta t = 0$), the simulations have already run for 1.5 ms from ad hoc initial conditions and are judged to be in a quasi-steady turbulent equilibrium.

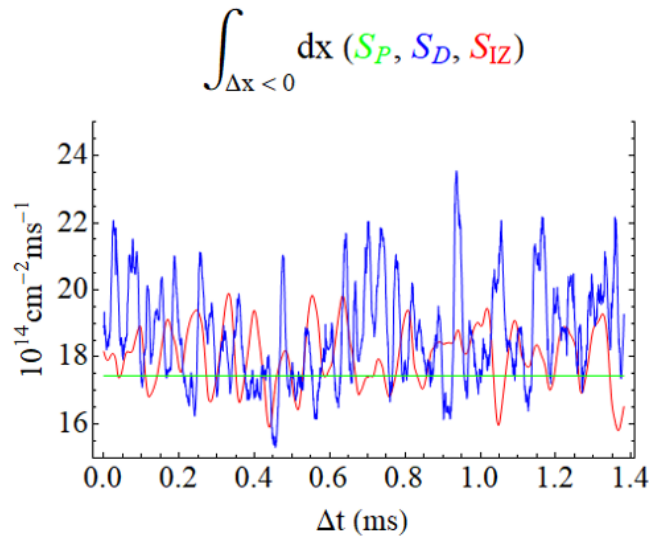


Fig. 2. Fueling rates, Eq. (8), for the three simulations. The simulations were run from ad hoc initial conditions for 1.5 ms, to allow transients to relax, prior to the start of the analysis of the equilibrium states which begins at $\Delta t = 0$ and continues for an additional 1.4 ms. Note the zero offset on the vertical scale. [Associated dataset available at <https://doi.org/10.5281/zenodo.4994177>]

With fueling rates synchronized, the simulation profiles are compared in equilibrium in Fig. 3. The profiles from the reference SOLPS simulation are shown as dashed curves. The fueling in the SOLPS simulation is dominated by divertor recycling, [24] and, as seen in Figs. 3(a) and 3(b), the density and electron temperature profiles from case D are in better agreement with the corresponding SOLPS profiles *in the SOL* than are those of the other two simulations. Despite differences between the n , T_e and T_i profiles, the pressure profiles in Figs. 3(d) and 3(e) are in good agreement, suggesting similar turbulent energy transport mechanisms at work in the simulations.

The neutral density profiles from the simulations, Fig. 3(f), are expected to differ from the SOLPS profile because the puffed case (IZ) uses a relatively large puff density to maintain the plasma density near the SOLPS profile without the benefit of divertor recycling, while cases D and P use relatively miniscule puffs for diagnostic purposes. Notice that the D and P neutral profiles are alike, suggesting similar SOL transparencies with respect to neutral penetration.

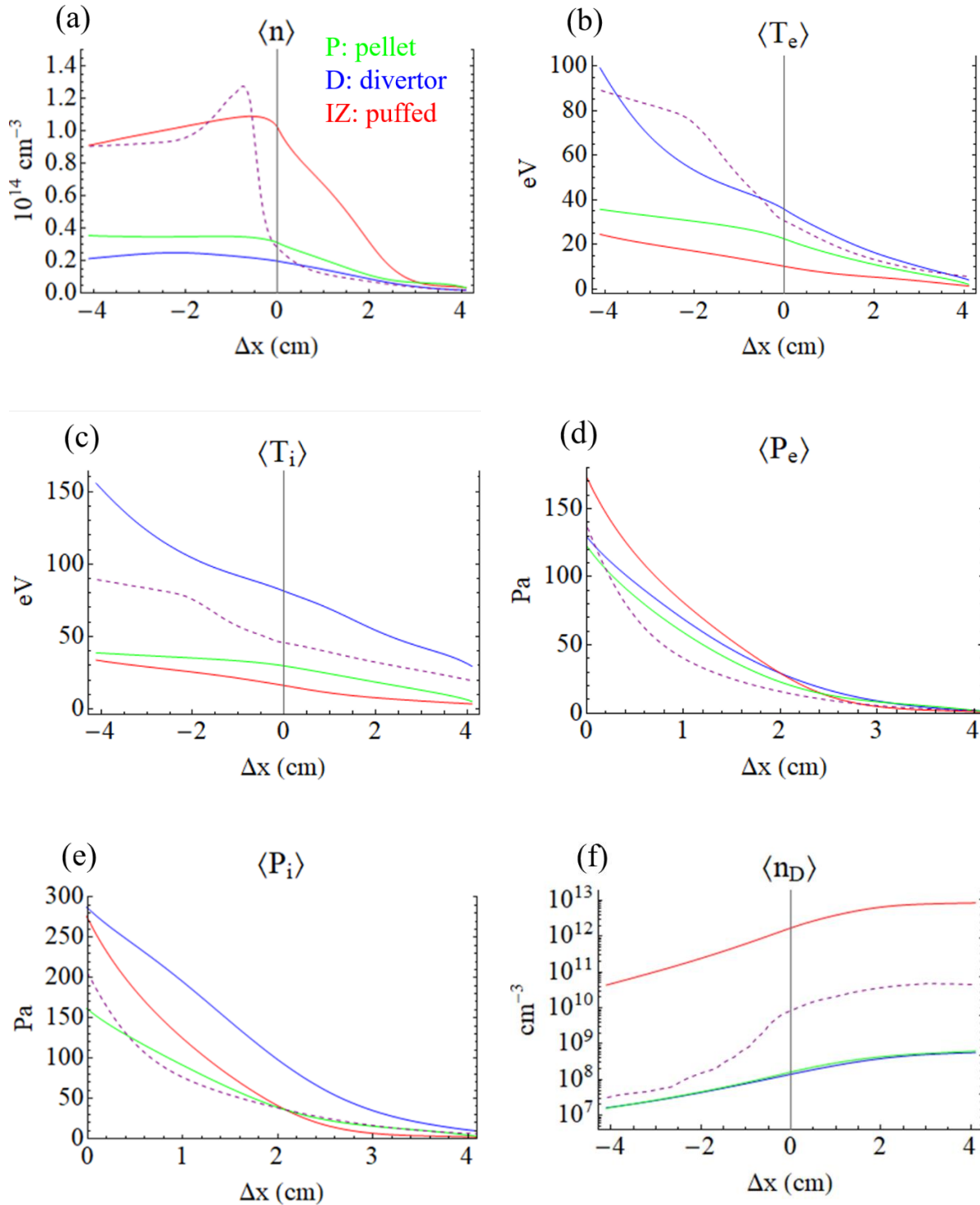


Fig. 3. Equilibrium profiles from the simulations. Angular brackets denote a y- and t-average. Profiles from a SOLPS simulation of an H-mode, for conditions illustrative of MAST-U, are shown dashed for reference. The pronounced “ear” in the SOLPS density profile results from a trench in the SOLPS D_n profile used to simulate the H-mode. The nSOLT simulations are presumed to be in L-mode. [Associated dataset available at <https://doi.org/10.5281/zenodo.4994177>]

IV. SOL transparency and fueling efficiency

To measure neutral penetration of the edge region, we distinguish between SOL transparency (ST) and the fueling efficiency (FE). We define the former as the ratio of the density of neutrals at the separatrix that are headed for the core ($v_x < 0$) to the density of neutrals sent into the SOL from the wall, viz.,

$$ST = \int_{v_x < 0} dv_x G(\Delta x = 0, v_x) / \int_{v_x < 0} dv_x G(x = L_x, v_x), \quad (9)$$

and the fueling efficiency to be the ratio of neutral *fluxes* similarly restricted:

$$FE = \int_{v_x < 0} dv_x v_x G(\Delta x = 0, v_x) / \int_{v_x < 0} dv_x v_x G(x = L_x, v_x). \quad (10)$$

The phase space portrait of the neutral particle flux is shown in Fig. 4 for the puffed case.

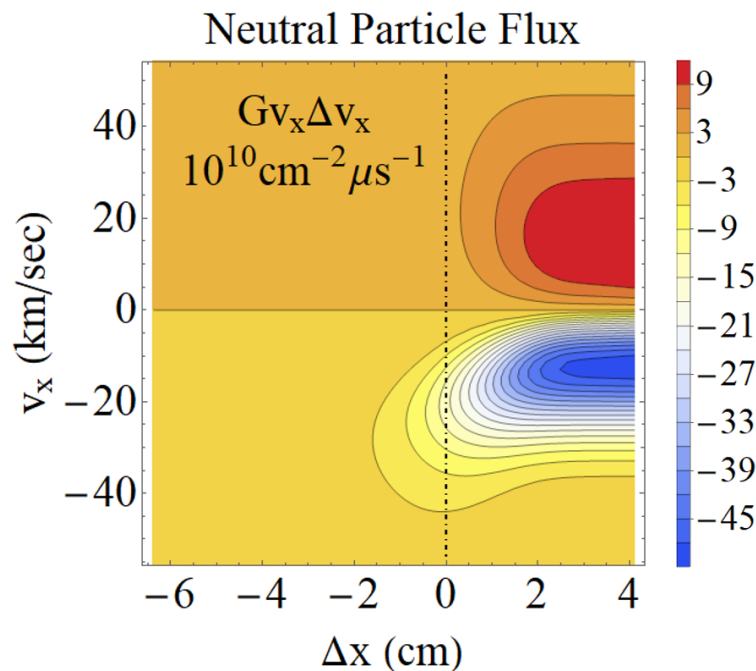


Fig. 4. Phase space ($\Delta x, v$) contour plot of the neutral particle flux density, $Gv_x \Delta v_x$, in the puffed case. The blue feature indicates injected neutrals moving away from the wall and into the edge

and near-SOL where they are heated by charge-exchange and lost to ionization. The red feature indicates CX-heated neutrals moving toward the wall from the edge and near-SOL. [Associated dataset available at <https://doi.org/10.5281/zenodo.4994177>]

The SOL transparencies and fueling efficiencies are compared for the three cases in Table I. To within standard deviations, cases D and P are indistinguishable, with SOL transparencies $\sim 25\%$ and fueling efficiencies $\sim 50\%$; one quarter of the injected neutrals survive ionization in the SOL to reach the separatrix (as neutrals) and arrive there with twice the velocity with which they were launched from the wall, on average. [The ratio of FE Eq. (10) to ST Eq. (9) is $FE/ST = \langle v_x \rangle(\Delta x=0) / \langle v_x \rangle(x=L_x)$.]

In the puffed case, the SOL transparency is 22% and the fueling efficiency is 40%. This case has the largest plasma density and the smallest electron temperature in the SOL. However, the transparency is only slightly reduced from that found for cases P and D. The neutral ionization rates in the SOL are compared in Fig. 5(a). The lower temperature and higher electron density in the puffed case apparently offset each other to yield an ionization rate close to those of the other two cases.

The charge-exchange rate is only weakly dependent on the ion temperature [cf. Eq. (4c)] and is largest in the puffed case due to the larger electron density in the SOL. See Fig. 5(b). This relatively rapid exchange of energy with significantly cooler ions accounts for the reduced fueling efficiency, i.e., slower neutrals at the separatrix, compared to the other two cases.

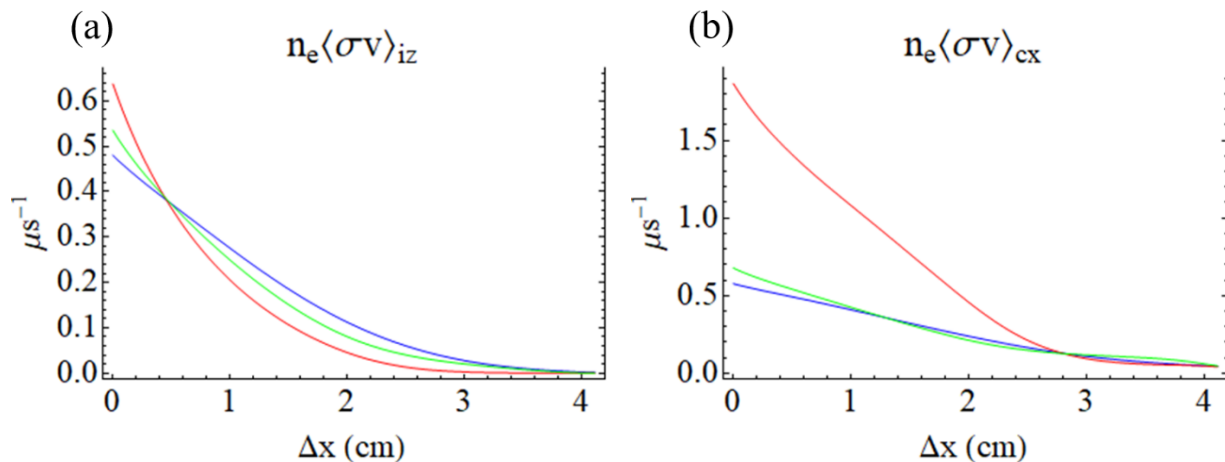


Fig. 5. Ionization (a) and charge exchange (b) rate profiles in the SOL. [Associated dataset available at <https://doi.org/10.5281/zenodo.4994177>]

The effect of charge exchange heating of the neutrals is evident in Fig. 4, where the phase-space (x, v_x) contours of the neutral particle flux broaden to larger velocities in the near-SOL and edge regions. The pronounced red feature for $v_x > 0$ indicates CX-heated neutrals, made in the edge and near-SOL, free-streaming to the wall. The *energy* flux at the wall due to these returning neutrals is 110 kW/m² in the puffed case ($n_{\text{puff}} = 10^{13} \text{ cm}^{-3}$) and is comparatively negligible in the P and D cases due to the much smaller “diagnostic” puff density (10^9 cm^{-3}). However, the *ratios* of the exiting energy flux ($v_x > 0$) to the injected energy flux ($v_x < 0$) at the wall are 4.3, 1.5 and 1.2 in the D, P and IZ cases, respectively, and reflect the ordering of the ion temperatures in the near-SOL and edge where the returning CX-heated neutrals originate [cf. Fig. 3(c)].

fueling method	F (8)	ST (9) (%)	FE (10) (%)	$\lambda_{q,e}$ (11) (mm)	$\lambda_{q,i}$ (11) (mm)	P_{SOL} (12a) (MW)	P_{div} (12b) (MW)	P_{loss} (12c) (MW)
P pellet	17.4 ± 0.0	27.9 ± 2.6	48.5 ± 3.0	8.0 ± 0.6	12.3 ± 0.8	2.5 ± 0.6	2.4 ± 0.3	10^{-4}
D recycling	18.5 ± 1.5	25.3 ± 1.7	49.4 ± 2.0	7.7 ± 0.8	15.2 ± 1.2	6.6 ± 0.9	6.6 ± 0.6	10^{-4}
IZ puffed	18.1 ± 0.9	22.1 ± 1.9	39.8 ± 2.4	8.5 ± 0.3	9.4 ± 0.4	2.4 ± 0.3	1.8 ± 0.2	0.66 ± 0.03

Table I. Measured average quantities for the pellet (P), divertor (D) and puff-fueled (IZ) simulations. Measurements are of the form $m \pm \text{s.d.}$, where m denotes the time-average (mean), and s.d. is the standard deviation about the mean. Numbers in parentheses reference the equations defining the measurement. The fueling rate (F) is given in units of $10^{14} \text{ cm}^{-2} \text{ ms}^{-1}$.

V. Parallel energy flux and power budget in the SOL

Electron and ion parallel energy flux profiles in the SOL are shown in Fig. 6. (Expressions for the fluxes are given in Appendix A.) The corresponding Loarte heat flux widths [29],

$$\lambda_q = \int_{\Delta x > 0} \langle Q_{\parallel} \rangle dx / \langle Q_{\parallel}(\Delta x = 0) \rangle, \quad (11)$$

are given in Table I. Larger widths are preferable for spreading the heat loading over a larger area of the divertor and so prolonging its lifetime. The simulated heat flux widths are similar to those typically measured in MAST. [30]

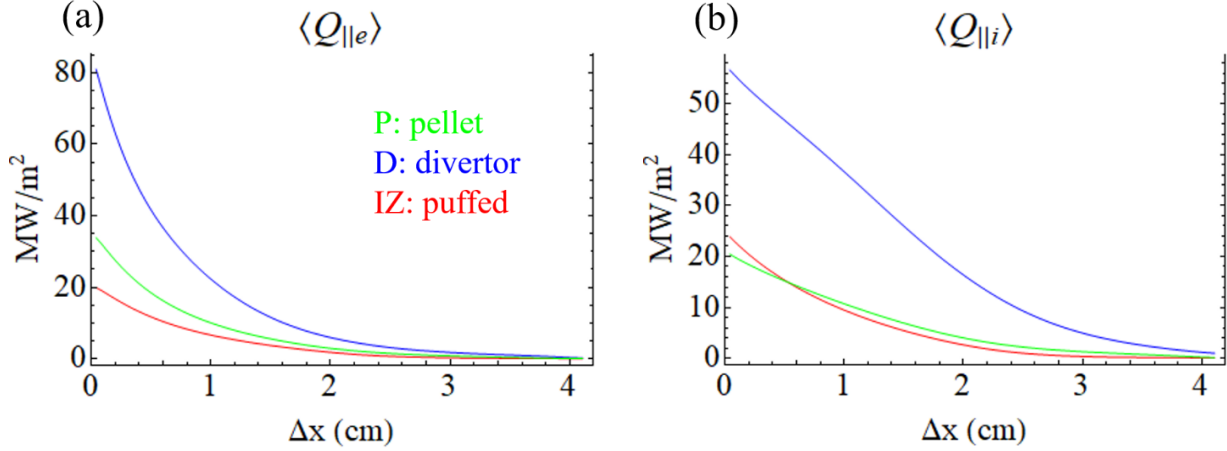


Fig.6. Electron (a) and ion (b) parallel heat flux profiles, Eqs. (A23) and (A24), in the SOL ($\Delta x > 0$). Angular brackets denote the y- and t-average. The corresponding heat flux widths (λ_q) are given in Table I. [Associated dataset available at <https://doi.org/10.5281/zenodo.4994177>]

The plasma power crossing the separatrix from the edge (P_{SOL}) is [cf. Eqs. (2)]

$$P_{\text{SOL}} = 2\pi R_m \int dy \left(v_{\text{Ex}} \frac{3}{2} n T_e - \chi_e n \partial_x T_e + v_{\text{Ex}} \frac{3}{2} n T_i - \chi_i n \partial_x T_i \right) \Big|_{\Delta x=0}, \quad (12a)$$

i.e., the radial energy flux at the separatrix integrated over the last closed flux surface.

P_{SOL} must equal the power lost along field lines to the divertor plate (P_{div}) plus the power lost to ionization and charge exchange in the SOL (P_{loss}), viz., $P_{\text{SOL}} = P_{\text{div}} + P_{\text{loss}}$,

where

$$P_{\text{div}} = 2\pi R_m b_\theta \int_{\Delta x > 0} dx (\bar{Q}_{||e} + \bar{Q}_{||i}), \quad (12b)$$

and

$$P_{\text{loss}} = 2\pi R_m \int_{\Delta x > 0} dx dy [\langle \sigma v \rangle_{iz} n_0 n E_{iz} - (\langle \sigma v \rangle_{iz} + \langle \sigma v \rangle_{cx}) n_0 n E_0 + \frac{3}{2} \langle \sigma v \rangle_{cx} n_0 n T_i]. \quad (12c)$$

Here the ratio of poloidal to total magnetic field strength is $b_\theta = B_p/|\mathbf{B}| = 0.545$ for the MAST-U OM.

In practice, the y-integrals in Eqs. (12a) and (12c) are replaced with $L_\theta \langle f \rangle_y$, where f stands for either integrand, and L_θ is an effective domain length chosen by demanding that $P_{\text{SOL}} = P_{\text{div}}$ when the turbulence is in steady state and there is no loss due to ionization in Eqs. (2). See

Appendix B for details. This device allows the computation of volume integrated quantities from the 2D simulation.

The time-averaged total powers (P_{SOL}) are given in Table I. The fraction of P_{SOL} in the electron channel is 0.42, 0.40 and 0.51 for D, IZ and N, respectively, and the remainder is in the ion channel. Only in the puffed case is P_{loss} significant and important for power conservation, amounting to 25% of the power entering the SOL. Although the recipe for L_0 , Eq. (B3), ignores P_{loss} , it nevertheless gives good power conservation in the puffed case.

Case D has significantly more input power than the other two cases, and it is the case characterized by the strongest turbulence, as discussed next.

VI. Characteristics of the fluctuations

Contour plots of the electrostatic potential and fractional density fluctuation and are shown in Figs. 7 at the end of the puffed simulation. In all cases, the potential fluctuations consist of separatrix-spanning cells, centered in the edge region, about which the plasma tends to rotate clockwise. These “vorticity cells” are most persistent in the puffed case. Blobs are emitted intermittently from the regions between the cells, in a neighborhood of the separatrix, and propagate into the SOL. We have occasionally seen blobs get emitted from the top of a cell only to be sucked back into the edge at the bottom. Similar separatrix-spanning convective cells were also observed in previous simulations of the NSTX device using the SOLT code (where neutral physics was not modeled). [31] Radial profiles of the time-averaged fluctuation amplitudes are shown in Figs. 8. The cases are ordered by fluctuation amplitude according to $D > P > \text{IZ}$ in the far-edge and near-SOL ($-2 \text{ cm} < \Delta x < 2 \text{ cm}$).

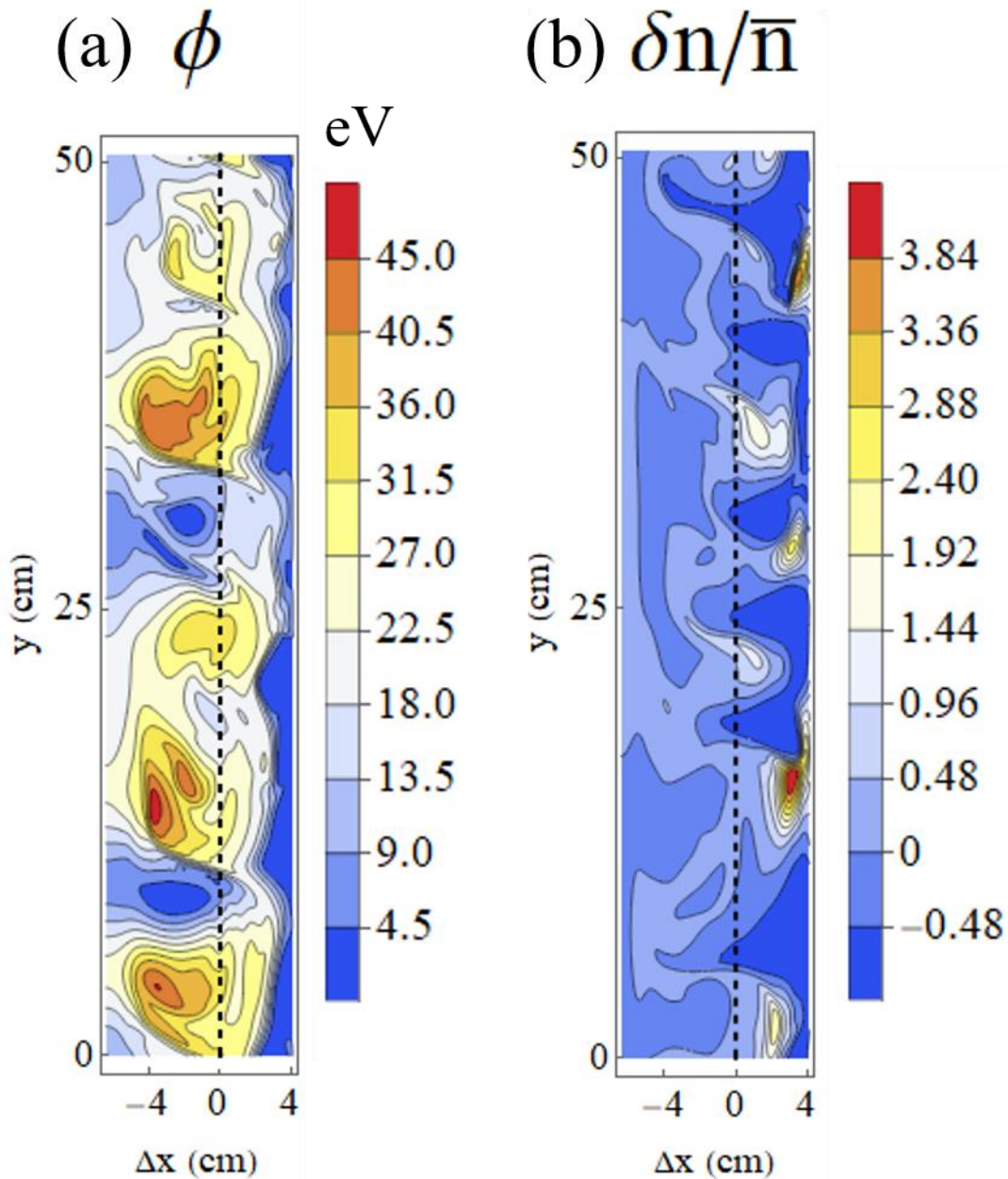


Fig. 7. Contour plots of (a) the electrostatic potential (ϕ) and (b) the fractional density fluctuation ($\delta n / \bar{n}$, $\bar{n} \equiv \langle n \rangle_y$), for the puffed (IZ) case. Notice the separatrix-spanning vortex cells in (a) and the blobs in the SOL in (b). Plasma flows around the cells in the clockwise direction. Blobs are ejected from the canals between the cells. [Associated dataset available at <https://doi.org/10.5281/zenodo.4994177>]

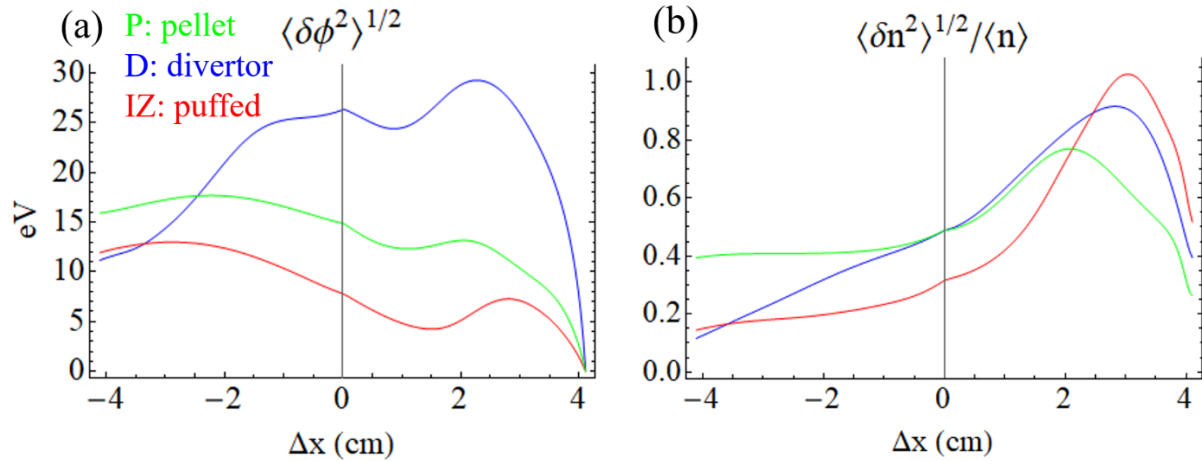


Fig.8. Profiles of (a) electrostatic potential fluctuations and (b) plasma density fluctuations, divided by the mean density, for the simulations. Angular brackets denote a y- and t-average. [Associated dataset available at <https://doi.org/10.5281/zenodo.4994177>]

Profiles and histories of the radial turbulent particle flux are shown in Figs. 9. The similar magnitude of the particle fluxes crossing the separatrix for the three fueling scenarios is expected since the source rates in the closed surface region have been chosen to be approximately equal. Fluctuations of the flux at the separatrix are $\sim 50\%$ of the mean value, and they have a periodic component, particularly apparent in the puffed and pellet-injected cases, at roughly 10 kHz. The power spectra of the potential and density fluctuations at the separatrix are maximized at $\omega/2\pi \sim 10$ kHz, and this frequency is consistent with the rotation rate that may be inferred from the snap shot of ϕ in Fig. 7(a), as discussed below.

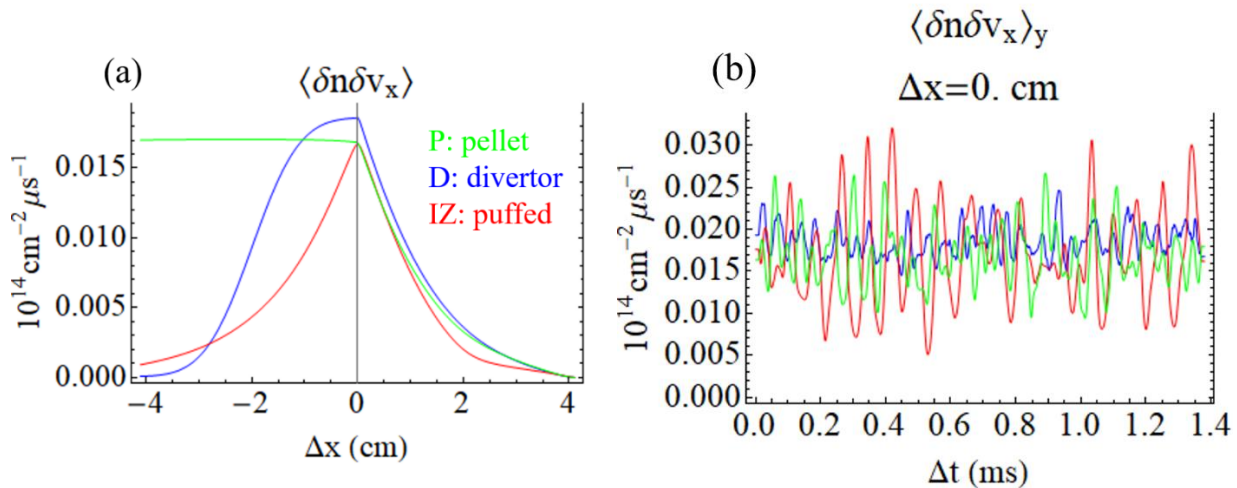


Fig. 9. Profiles (a) and histories (b) of the particle turbulent flux ($\delta n \delta v_x$). In (b), a strong periodic component (~ 10 kHz), particularly evident in the puffed case, corresponds to rotation about the vortex cells in Fig. 7(a). The angular brackets denote a y- and t-average in (a). [Associated dataset available at <https://doi.org/10.5281/zenodo.4994177>]

The skewness of the density fluctuations,

$$skewness = \left\langle \left\langle \delta n^3 \right\rangle_y / \left\langle \delta n^2 \right\rangle_y^{3/2} \right\rangle_t \quad (13)$$

is plotted in Fig. 10(a). Where it passes through zero, changing from negative to positive, the character of the fluctuations changes from hole to blob, suggesting a blob birth-zone in the near-SOL ($0 < \Delta x < 2$ cm) for all cases. The canonical blob propagation picture, [32] in which the grad-B and curvature drifts polarize the blob poloidally [cf. the term $\sim \kappa$ in Eq. (3b)] and the resulting $\mathbf{E}_y \times \mathbf{B}$ drift propels the blob radially outward, is only weakly supported by cross-phase measurements,

$$cross-phase = \left\langle \left\langle \delta E_y \delta n \right\rangle_y / \left(\left\langle \delta E_y^2 \right\rangle_y^{1/2} \left\langle \delta n^2 \right\rangle_y^{1/2} \right) \right\rangle_t, \quad (14)$$

plotted in Fig. 10(b), where perfect blob polarization corresponds to a value of unity. The circulation associated with the vortex cells in Fig. 7(a) likely obscures relatively occasional blob emission in the cross-phase diagnostic. Both cross-phase and skewness are consistent with the picture of blobs piling up in the far-SOL [Fig. 7(b), $\Delta x > 2$ cm]: connection to the divertor sheath improves with decreasing $L_{\parallel}(x)$ moving away from the separatrix, and blob rotation (i.e. ‘spin’ from ∇T_e sheath-induced monopole blob potential profiles) replaces radial translation. [32]

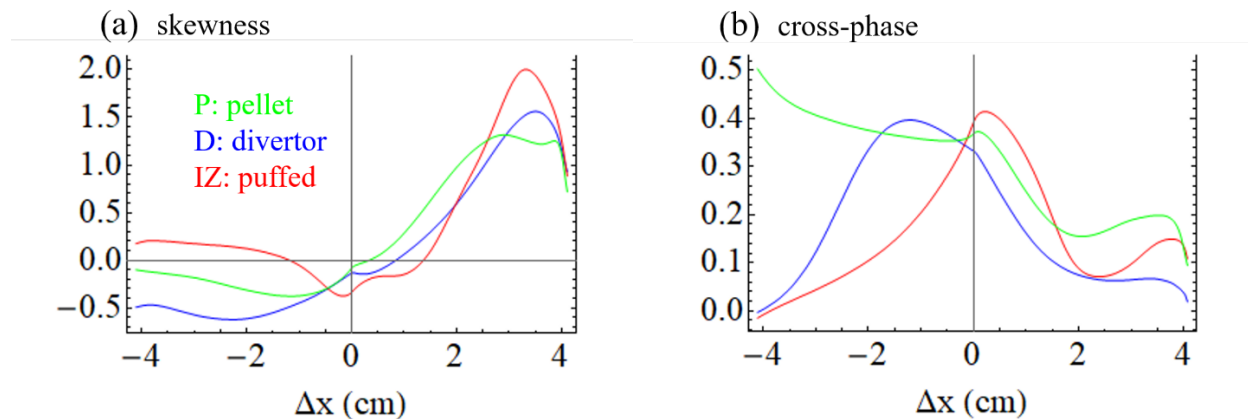


Fig. 10. Profiles of (a) the skewness of density fluctuations, Eq. (13), and of (b) the cross-phase between density fluctuations and poloidal electric field fluctuations, Eq. (14). The blob birth zone is found where the skewness passes through zero on $0 < \Delta x < 2$ cm. The cross-phase decreases in the birth zone as blob translation changes to rotation with decreasing parallel connection length and increasing connection to the divertor sheath. [Associated dataset available at <https://doi.org/10.5281/zenodo.4994177>]

If there is an underlying linear instability driving the turbulence in these simulations, it must be the curvature-interchange (C-I), drift wave, Kelvin-Helmholtz (K-H) or sheath instability that can be active in the nSOLT model. However, only the C-I and K-H instabilities are candidates to underly the turbulent transport in the edge and near-SOL. The C-I instability growth rate is $\gamma_{\text{mhd}} = \left[-\beta \partial_x (\bar{P}_e + \bar{P}_i) / \bar{n} \right]^{1/2}$, where the radicand is positive, and $\beta = 2\rho_{\text{sr}}/R_m$. The K-H instability growth rate is a fraction of the magnitude of the flow shearing rate, $\xi \equiv \partial_x \bar{v}_{E_y}$. Profiles of the two rates are compared in Fig. 11 for the three cases, and it is seen that $|\xi|$ and γ_{mhd} are comparable in the birth zone ($0 < \Delta x < 2$ cm) except in a neighborhood of the separatrix where $|\xi|$ is markedly larger.

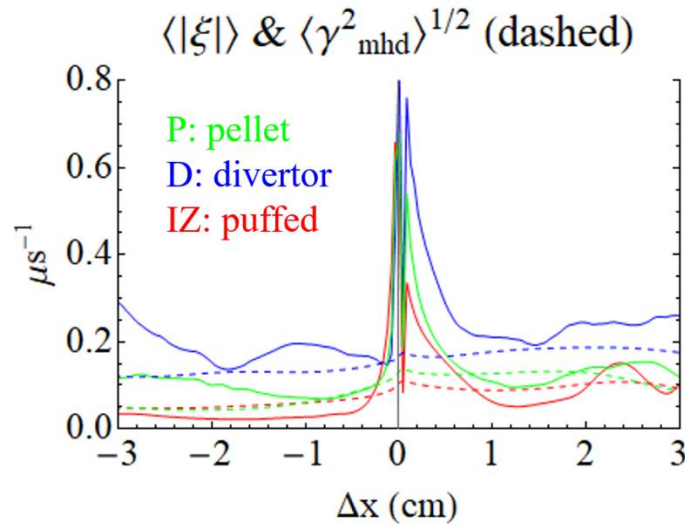


Fig. 11. Profiles of flow shearing rate, $\xi \equiv \partial_x \bar{v}_{E_y}$, and of the interchange growth rate, $\gamma_{\text{mhd}} = \left[-2(\rho_{\text{sr}} / R_m) \partial_x (\bar{P}_e + \bar{P}_i) / \bar{n} \right]^{1/2}$ (dashed), superimposed for the simulations. The over-bar denotes the y-average, and the angular brackets denote the time-average. The flow shearing may control the interchange instability, i.e., $|\xi| \sim \gamma_{\text{mhd}}$, in the birth zone, and the large shearing rate near the separatrix may act as a transport barrier. [Associated dataset available at <https://doi.org/10.5281/zenodo.4994177>]

In studies of the K-H instability driven by a jump-discontinuous velocity profile [33], it was found that the growth rate of the K-H instability was a fraction of the shearing rate, $\gamma_{\text{KH}} \sim 0.2 |\xi|$. If a similar reduction were appropriate for the present simulations, then the interchange instability would dominate the K-H instability in the birth zone, based on the time-averaged profiles. The fact that $\gamma_{\text{mhd}} \sim |\xi|$ suggests, however, that the sheared flow is moderating the interchange instability in the birth zone. [34] Features of the energy and power spectra are consistent with a turbulent equilibrium driven by the interchange instability, as we discuss next.

Energy (k_y) spectra of the fluctuations at the separatrix are shown in Fig. 12. The energy spectra of the potential fluctuations ($\delta\phi$) are maximized at poloidal mode number $m_y = k_y L_y / (2\pi) = 4$ in all cases, corresponding to the vortex cells seen in Fig. 7(a). Energy spectra of the density fluctuations (δn) are maximized at mode number $m_y = (4, 5, 4)$ in case (D, IZ, P) corresponding to $k_y \sim 0.5 \text{ cm}^{-1}$. Thus, $1/k_y \sim 2 \text{ cm}$ which is similar to the radial scale lengths of the profiles in Fig. 3, as expected from linear interchange instability considerations, i.e., $k_y L_n \sim 1$ at maximum growth rate. All energy spectra fall off exponentially at high- k_y . The cases are ordered by potential fluctuation energy according to $D > P > \text{IZ}$, and the ordering is reversed, i.e., $\text{IZ} > P > D$, for the density fluctuations. This reversal is not overly surprising since the particle fluxes crossing the separatrix, which scale like the product $\delta v_x \delta n \sim \delta\phi \delta n$, must be equal to the core fueling rate common to all cases. If the δn spectra are divided by their corresponding mean-field energies then the ordering observed at the separatrix in Fig. 8(b) is recovered: $P \sim D > \text{IZ}$, as it should be since from continuity, we expect $\delta\phi \sim \delta n/n$.

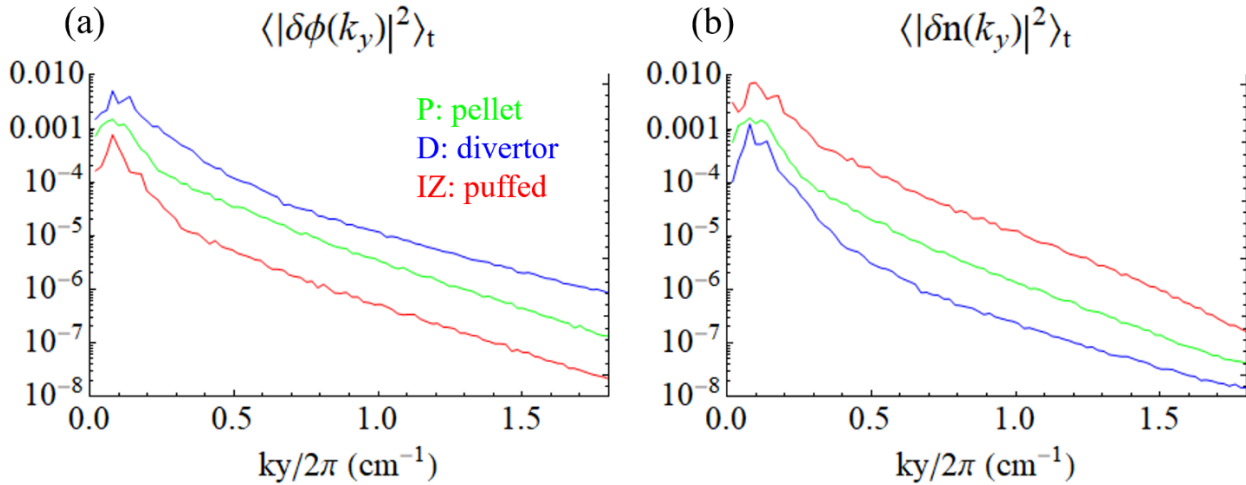


Fig. 12. Potential (a) and plasma density (b) energy (k_y) spectra at the separatrix. Maxima in the potential spectra are found at $k_y L_y / (2\pi) = 4$ in all cases, corresponding to the vortex cells seen in Fig. 7(a). The fluctuations are given in dimensionless (Bohm) units. [Associated dataset available at <https://doi.org/10.5281/zenodo.4994177>]

Power (ω) spectra, averaged over eight poloidal “probe” locations at the separatrix, are shown in Fig. 13. A break in the slope of the density spectra, or “knee,” is apparent in the neighborhood $10 \text{ kHz} < \omega/2\pi < 30 \text{ kHz}$, where the spectra transition from discrete spikes to the relatively smooth power-law fall-off ($\sim \omega^{-p}$) indicative of a cascade. The interchange growth rates in the birth zone, $16 \text{ kHz} < \gamma_{\text{mhd}}/2\pi < 32 \text{ kHz}$, cf. Fig. 11, lie within this knee, supporting the observation that the interchange instability is driving the turbulence. This *injection* range of frequencies is also consistent with the time scale of the perpendicular transport inferred from the blob dispersion relation for order unity fluctuations, viz.,

$$\gamma_{\text{mhd}} \delta n \sim \frac{\delta v_{\text{Ex}}}{L_{\perp}} \bar{n}, \text{ with } \delta n \sim \bar{n},$$

and it is consistent, as it must be, with the parallel loss rate, c_s/L_{\parallel} , in the SOL: (25, 11.8, 16.7) kHz for (D, IZ, P) at $\Delta x = 1$ cm.

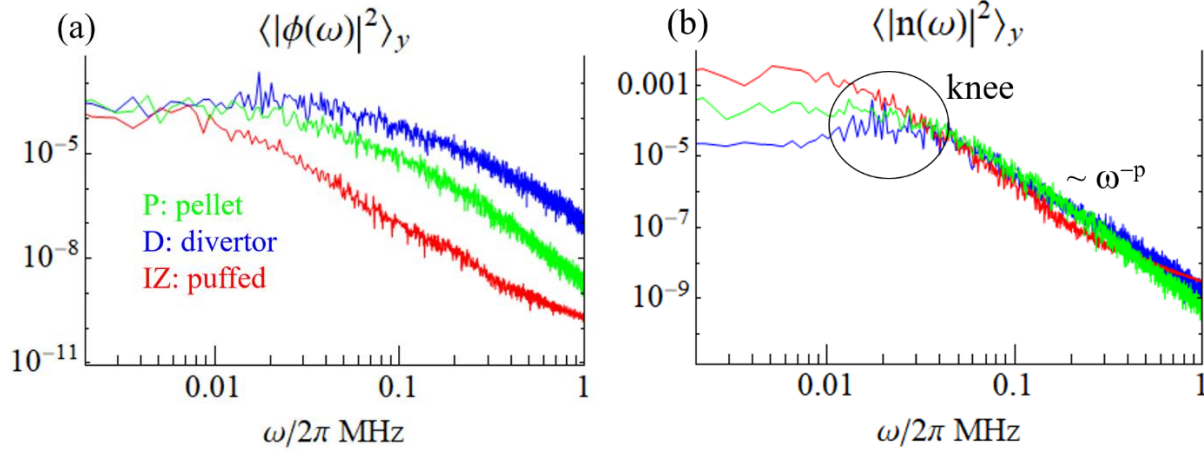


Fig. 13. Power (ω) spectra averaged over eight poloidal “probe” locations at the separatrix. A “knee” forms in the density power spectra (b) where interchange growth rates (γ_{mhd}), which characterize perpendicular transport rates, parallel loss rates (c_s/L_{\parallel}) and cell rotation rates coincide. The resolution is $\Delta\omega/2\pi = 724/\text{sec}$. [Associated dataset available at <https://doi.org/10.5281/zenodo.4994177>]

The injection frequencies are also factor-of-two consistent with the oscillations apparent in Fig. 9(b) and with rotation rates inferred from the snap shots of the potential fluctuations in Fig. 7(a). For example, in the upper cell for the puffed case (IZ), the potential decreases by 10 eV in 2 cm. In local polar coordinates, and in physical units,

$$v_{\theta} = \frac{c}{B} \frac{\partial \phi}{\partial r} = 0.875 \text{ km/sec}.$$

So, with $\omega = v_{\theta}/r = 0.875 \text{ km/sec}/(2 \text{ cm})$, we find that $\omega/2\pi = 6.96 \text{ kHz}$, compared to 7.2 kHz for the peak in the potential power spectrum.

Except for the $\delta\phi$ spectra in the D and P cases, the spectra fall off like power laws ($\sim\omega^{-p}$) at high- ω . Power spectra in the far-SOL (not shown) are similar to those shown in Fig. 13. Power-law spectra are predicted for Poisson-distributed waiting times between successive blob arrivals, [35] but our blob sample size is insufficient in the far-SOL to explore this prediction, and the invariance of spectra with radial location suggests that there may be a different explanation for the power-law fall-off observed here.

VII. Summary and concluding remarks

We have simulated plasma turbulence in the outboard midplane region of the tokamak with the nSOLT reduced model turbulence code for three distinct fueling methods: pellet injection (P), divertor recycling (D) and neutral puff injection (IZ). Aside from those which define the fueling sources, all parameters were held fixed across the three simulations and were chosen to be illustrative of conditions anticipated in the MAST-U device. By adjusting the parameters of the fueling sources in the plasma density evolution equation, the fueling rates in each simulation were tuned to agree, and the three cases were compared in a quasi-steady turbulent equilibrium. The target fueling rate was chosen so that the nSOLT density and electron temperature profiles in the SOL agreed reasonably well with those observed in a SOLPS transport simulation of an H-mode at MAST. [24]

Diagnostics applied to the simulations include SOL transparency to puffed neutrals and neutral fueling efficiency, parallel heat flux width (λ_q) in the SOL, and diagnostics of the turbulent fluctuations including skewness, cross-phase, and power spectra. Several diagnostic measures are summarized in Table I.

A common turbulent transport mechanism appears to be at work in all cases. The equilibrium turbulent fluctuations consist of wobbling, separatrix-spanning vorticity cells, centered in the edge, about which the plasma circulates, intermittently ejecting blobs into the SOL. The electron pressure profiles are in good agreement in the SOL, as are time-averaged particle fluxes at the separatrix. Pellet fueling and divertor recycling present the same SOL to neutral penetration and fueling efficiency, as measured by a weak, “diagnostic” neutral puff. Pellet fueling and puffing produce the same parallel heat flux profiles and send the same power across the separatrix (but *not* the same power, P_{div} , to the divertor). The density fluctuation power spectra agree at high frequencies in all cases. Despite these similarities, there are important difference between the cases.

The *puffed case* has the largest plasma density, and the smallest plasma temperatures due to ionization and charge-exchange cooling. It has the smallest electron parallel heat flux in the SOL, spread over the largest electron heat flux width. It has the smallest ion heat flux width, with parallel heat flux comparable to that observed for pellet injection. It has the smallest power crossing the separatrix, P_{SOL} , though comparable to that observed for pellet injection (2.5 MW). However, due to IZ and CX losses in the SOL, *it sends the least power to the divertor* (1.8 MW).

The puffed case is also the least turbulent case: It has the smallest turbulent fluctuation amplitudes (potential and density) in the edge and near-SOL, and it has the smallest flow shearing rates and interchange instability growth rates in the edge and SOL. In other words, neutral puff fueling elicits a relatively muffled turbulent response from the plasma dynamics and, either through the consequently reduced Reynolds-stress production of sheared mean flow and/or neutral-friction drag on the mean flow, opposes the formation of high-shear layers that are observed in the other two cases. This interpretation is consistent with the conjectured role of neutrals in impeding the L-H transition in NSTX, inferred from the improved access to that transition when lithium was used to reduce neutral recycling. [36]

Divertor-recycling produces the smallest plasma density, the largest plasma temperatures, the largest parallel heat fluxes and the largest ion heat flux width in the SOL. This is the case that sends the greatest heat flux to the divertor.

Divertor-recycling produces the strongest turbulence: It has the largest potential fluctuation ($\delta\phi$) amplitudes everywhere and the largest normalized density fluctuations in the near-SOL and far-edge. It has the largest shearing rates and interchange growth rates in the edge and SOL. Despite this, the system necessarily organizes itself so that the turbulent particle flux crossing the separatrix is essentially equal to that in the puffed and divertor-recycled cases, balancing the common source rates.

Although the space and time average plasma profiles are significantly different in all three cases, our main conclusion is that the resulting calculated fueling efficiencies, SOL transparencies and many of the turbulent properties such as skewness and cross-phase profiles, energy and power spectra and characteristic frequencies are remarkably similar. The fueling method, whether it be deep in the core, on the closed flux surfaces near the separatrix or in the SOL, seems not to have a great impact on these quantities when the turbulence and profiles are allowed to reach a quasi-steady state that is self-consistent with the fueling. This answers the main question motivating our paper.

A secondary result, of more general interest, is the relationship between linear growth rates, turbulent time scales and the parallel loss rate in the SOL. When (i) fluctuation amplitudes approach order unity, (ii) there is no spatial scale separation between “equilibrium” profiles and the fluctuations, and (iii) profiles evolve to a self-consistent quasi-steady state with the turbulence, several characteristic time scales in the problem merge. Considering the density field, the SOL density width (neglecting SOL particle sources) is set by equating the perpendicular and parallel transport terms: perpendicular transport from the separatrix balances parallel losses. Thus, we expect $1/\tau_{\parallel} = c_s/L_{\parallel}$ to balance $1/\tau_{\perp} \sim (k_{\perp} \delta v_E) \sim \gamma$ where the final estimate follows from the continuity equation for fluctuations, while the turbulent time scale for transport τ_{\perp} is estimated from $1/\tau_{\perp} \sim \Gamma_{\perp}/L_{\perp} \sim (\delta n/n)\delta v_E/L_{\perp} \sim \delta v_E/L_{\perp}$. These estimates, applying when the instability mechanism is dominated by convection (e.g. the interchange mechanism) are consistent with the observed similarity of the vortex cell rotation period, the parallel loss time, the fluctuation spectral peaks, and the interchange growth time.

Finally, our work emphasizes the importance, already broadly recognized in the community, of turbulence simulations that not only include self-consistent sources and profile evolution, but also are able to compute out to sufficiently long time-scales that a quasi-steady turbulent state is actually achieved. To this end, reduced models such as the present one may, with presently available computational resources, offer some significant advantages in the quest for reliable simulations of fusion-relevant edge and SOL plasmas.

Acknowledgements

This material is based on work supported by the US Department of Energy Office of Science, Office of Fusion Energy Sciences under award numbers DE-FG02-97ER54392 and DE-SC0019270.

Data Availability Statement

The data that support the findings of this study are openly available in Zenodo at <https://doi.org/10.5281/zenodo.4994177>.

Appendix A Parallel transport

The plasma parallel current density (j_{\parallel}), particle flux (Γ_{\parallel}) and heat fluxes ($Q_{e\parallel}$ and $Q_{i\parallel}$) are based on models of electrostatic drift wave physics in the core region and of divertor sheath physics (via ‘‘closure’’ relations) in the SOL. These are dynamical quantities that evolve with the turbulent plasma fields. The forms of these fluxes have been modified since they were last given in reference [23] and differ somewhat from those used in [16]. Here we give the forms used in the simulations reported in this paper. The parallel flux gradients appearing in the model equations, viz., $\nabla_{\parallel}\Gamma_{\parallel e}$ [Eq. (1)], $\nabla_{\parallel}Q_{\parallel e}$ [Eq. (2a)], $\nabla_{\parallel}Q_{\parallel i}$ [Eq. (2b)] and $\nabla_{\parallel}j_{\parallel}$ [Eq. (3b)] have different forms on open and closed field lines, and we discuss them separately in sections A.1 and A.2 respectively below. The expressions are summarized in section A.3. Expressions are given in Bohm units, unless specified otherwise.

A.1 Open field lines

On the open field lines in the SOL ($x > x_{\text{sep}}$), the total current *at the sheath entrance* is given by a Padé interpolation [23] of limiting forms of the particle fluxes based on those given in [37].

$$j_{\text{Padé}} = \left[\left(\Gamma_{\parallel i\text{SL}} - \Gamma_{\parallel e\text{SL}} \right)^{-1} - \Gamma_{\parallel e\text{CL}}^{-1} - \Gamma_{\parallel e\text{FL}}^{-1} \right]^{-1}, \quad (\text{A1})$$

where the sheath-limited (SL), conduction-limited (CL) and (thermal) flux-limited (FL) fluxes are

$$\Gamma_{\parallel e\text{SL}} = nc_s \exp \left[\frac{\phi_B - \phi}{T_e} \right], \quad (\text{A2})$$

$$\Gamma_{\parallel e\text{CL}} = -1.96 \frac{\Omega_e}{v_{ei0}} T_e^{5/2} \left(\frac{\phi - \phi_B}{T_e} \right) L_{\parallel}(x), \quad (\text{A3})$$

$$\Gamma_{\parallel e\text{FL}} = 60 n T_e^{1/2}, \quad (\text{A4})$$

$$\Gamma_{\parallel i\text{SL}} = nc_s. \quad (\text{A5})$$

The ion current on the open field lines is $\Gamma_{\parallel iSL}$ (A5). So, with the total current given by (A1), the electron parallel flux is

$$\Gamma_{\parallel e} = -j_{\parallel e} = nc_s - j_{Padé}. \quad (A6)$$

In the sheath-limited fluxes, Eqs. (A2 and A5), the sound speed is $c_s = (T_e + T_i)^{1/2}$ and the Bohm potential $\phi_B = 3T_e$. A more accurate expression for ϕ_B is given by

$$\frac{e\phi_B}{T_e} = \ln\left(\frac{v_{Te}}{(2\pi)^{1/2}c_s}\right). \quad (A7)$$

This expression reduces to $3.18 - 0.5\ln(1 + T_i/T_e)$ for deuterium, which we approximate in our simulations by “3.”

In Eq. (A3) we have written the conduction-limited electron parallel current ($j_{\parallel eCL} = -\Gamma_{\parallel eCL}$) as $j_{\parallel eCL} = \sigma_{\parallel}E_{\parallel}$, where σ_{\parallel} is the Spitzer parallel conductivity, and approximated the electric field by $E_{\parallel} = -(\phi_B - \phi)/L_{\parallel}$, where $L_{\parallel} = L_{\parallel}(x)$ is the parallel connection length to the divertor sheath. (The electron-ion collision frequency, ν_{ei0} , and electron cyclotron frequency, Ω_e , are constants evaluated using the reference parameters in the simulations.)

The parallel flux *gradients* appearing in the model equations, Eqs. (1), (2) and (3b), are taken to be the averages of those gradients along the magnetic field line passing through (x,y) in the simulation plane. For example, the field-line average of $\nabla_{\parallel}\Gamma_{\parallel e}$, viz., $[\Gamma_{\parallel e}(z=L_{\parallel}) - \Gamma_{\parallel e}(z=0)]/L_{\parallel}$, is $\Gamma_{\parallel e}(z=L_{\parallel})/L_{\parallel}$ because we assume that the odd moments vanish in the simulation plane where the source of parallel flux (i.e., the turbulence) is concentrated. This effectively maps sheath boundary conditions into the plane, achieving “closure” and enabling a 2D model. $\Gamma_{\parallel e}(z=L_{\parallel})$ is the parallel flux at the divertor sheath entrance given in (A6). In the simulations, $L_{\parallel}(x) = a + b \text{Log}[(x - x_{sep})/\rho_{sr}]$, where a and b were determined from a fit to the connection lengths measured by field-line tracing in a magnetic reconstruction equilibrium. [24]

Defining α_{sh} to be the reciprocal of the connection length,

$$\alpha_{sh}(x) = 2\rho_{sr}/L_{\parallel}(x), \text{ (Bohm units)} \quad (A8)$$

we have

$$\nabla_{\parallel}\Gamma_{\parallel e} = \alpha_{sh}(x)\Gamma_{\parallel e}\left(1 - n_{floor}/n\right), \quad x > x_{sep} \quad (A9)$$

and

$$\nabla_{\parallel}\Gamma_{\parallel i} = \alpha_{sh}(x)\Gamma_{\parallel iSL}\left(1 - n_{floor}/n\right), \quad x > x_{sep}. \quad (A10)$$

With reference to the vorticity dynamics, Eq. (3b),

$$\nabla_{\parallel} j_{\parallel} = \alpha_{\text{sh}}(x) j_{\text{Padé}}, \quad x > x_{\text{sep}}, \quad (\text{A11})$$

with $j_{\text{Padé}}$ given by (A1). [The parameter n_{floor} is an ad hoc lower bound on the density imposed throughout the model for the sake of numerical expediency in the solution of the vorticity equation (3a).] In the present simulations $n_{\text{floor}}/n_{\text{r}} = 0.01$.

The electron *conductive* parallel heat flux on the open field lines, $q_{\parallel\text{e}}$, is a Padé interpolation of limiting forms and is given by

$$q_{\parallel\text{e}} = \left(q_{\parallel\text{SL}}^{-1} + q_{\parallel\text{CL}}^{-1} + q_{\parallel\text{FL}}^{-1} \right)^{-1}, \quad (\text{A12})$$

where

$$q_{\parallel\text{SL}} = c_{\text{E}} n_{\text{T}_e} c_{\text{s}} \exp\left[\frac{\phi_{\text{B}} - \phi}{T_{\text{e}}}\right], \quad (\text{A13})$$

$$q_{\parallel\text{CL}} = 3.2 T_{\text{e}}^{7/2} \frac{\Omega_{\text{e}}}{v_{\text{ei0}}} \frac{1}{L_{\parallel}(x)} \quad (\text{A14})$$

and

$$q_{\parallel\text{FL}} = 60 n_{\text{T}_e}^{3/2}. \quad (\text{A15})$$

In (A13), c_{E} is the sheath energy enhancement factor [37] which we take to be 2.5.

The total electron parallel heat flux gradient, cf., Eq. (2a), is the sum of the conductive ($\nabla_{\parallel} q_{\parallel\text{e}}$) and convective pieces, [22]

$$\nabla_{\parallel} Q_{\parallel\text{e}} = \left(\nabla_{\parallel} q_{\parallel\text{e}} + \frac{5}{2} T_{\text{e}} \nabla_{\parallel} \Gamma_{\parallel\text{e}} - 0.71 T_{\text{e}} \nabla_{\parallel} j_{\text{Padé}} \right) (1 - p_{\text{e},\text{floor}} / p_{\text{e}}), \quad x > x_{\text{sep}}, \quad (\text{A16})$$

with $\nabla_{\parallel} \rightarrow \alpha_{\text{sh}}(x)$. The ion parallel heat flux gradient is purely convective [22] in our model:

$$\nabla_{\parallel} Q_{\parallel\text{i}} = \frac{5}{2} T_{\text{i}} \nabla_{\parallel} \Gamma_{\parallel\text{i}} (1 - p_{\text{i},\text{floor}} / p_{\text{i}}), \quad x > x_{\text{sep}}. \quad (\text{A17})$$

The ion conductive heat flux, ($q_{\parallel\text{i}} = -\kappa_{\parallel\text{i}} \nabla_{\parallel} T_{\text{i}} \sim \frac{n T_{\text{i}}}{m_{\text{i}} v_{\text{i}}} \frac{T_{\text{i}}}{L_{\parallel}} \sim \frac{n T_{\text{i}}}{m_{\text{i}}} \frac{\lambda_{\text{i}}}{v_{\text{i},\text{th}}} \frac{T_{\text{i}}}{L_{\parallel}} = n T_{\text{i}} v_{\text{i},\text{th}} \frac{\lambda_{\text{i}}}{L_{\parallel}}$, where $v_{\text{i},\text{th}}$

is the ion thermal speed and $\lambda_{\text{i}} = v_{\text{i},\text{th}}/v_{\text{i}}$ is the ion mean free path) is deemed to be ignorable in comparison to the conductive flux, $\sim n T_{\text{i}} c_{\text{s}}$, to the extent that $\lambda_{\text{i}} \ll L_{\parallel}$, which we assume. Note that the ions are the species which always flows into the sheath in contrast to the electrons which are the sheath-reflected species. This results in the different forms for the ion and electron heat fluxes.

[The parameters $p_{e, \text{floor}}$ and $p_{i, \text{floor}}$ are consistent with the floors imposed on the density and temperatures in the model for the sake of i) numerical expediency in the solution of the vorticity equation (3a) and ii) tractability of the Boltzmann exponentials in (A2) and (A13).]

A.2 Closed field lines

On the closed field lines in the edge ($x \leq x_{\text{sep}}$), the model we take for the electron parallel particle flux is motivated by the electron drift wave model of Hasegawa and Wakatani. [38] The parallel current gradient is

$$\nabla_{//} j_{\parallel} = -\nabla_{//} \Gamma_{\parallel e} = \alpha_{\text{dw}}(x) \bar{T}_e^{3/2} \delta(\phi - T_e \ln(n)), \quad x \leq x_{\text{sep}}. \quad (\text{A18})$$

The overbar denotes the y-average of T_e in (A18) and $\delta(\dots)$ denotes a fluctuation. Thus, the flux-surface (y) average of the parallel gradient vanishes, as it must since $\langle \mathbf{B} \nabla_{\parallel} \mathbf{Q} \rangle_{\psi} = \langle \nabla \cdot (\mathbf{B} \mathbf{Q}) \rangle_{\psi} = 0$ for any quantity \mathbf{Q} , and in our model $\nabla_{\parallel} \mathbf{B}$ is neglected. The coefficient is proportional to the Braginskii electrical conductivity in the edge

$$\alpha_{\text{dw}}(x) = \frac{1.96 \Omega_e \rho_{\text{sr}}^2}{v_{\text{ei}} L_{\parallel, \text{turb}}^2} \tanh[(x_{\text{sep}} - x) / w_{\text{dw}}], \quad x \leq x_{\text{sep}}, \quad (\text{A19})$$

and zero in the SOL. We take $\alpha_{\text{dw}}(x)$ to decay to zero in the far-edge, reflecting the strong increase in collisionality, with decreasing T_e , near the separatrix. [The coefficient in (A19) is made of constant, reference parameters.] We take $w_{\text{dw}} = 1$ cm and the parallel scale length of the turbulence $L_{\parallel, \text{turb}} = 4\pi R_m$, as a reasonable approximation.

On the closed field lines, the electron parallel heat flux gradient, cf., Eq. (2a), is purely convective, [22]

$$\nabla_{\parallel} \mathbf{Q}_{\parallel e} = 3.21 \bar{T}_e \nabla_{//} \Gamma_{\parallel e}, \quad x \leq x_{\text{sep}}, \quad (\text{A20})$$

and we take the ion heat flux to be zero. Because $\nabla_{//} \Gamma_{\parallel e}$ has zero y-average on the closed field lines, cf. Eq. (A18), the parallel gradient (A20) does not survive averaging over a flux surface; there is no net plasma heating by drift waves on the closed flux surfaces in our model.

A.3 Summary

$$\nabla_{//} \Gamma_{\parallel e} = \begin{cases} -\alpha_{\text{dw}}(x) \bar{T}_e^{3/2} \{\phi - T_e \ln(n)\}, & x \leq x_{\text{sep}} \\ \alpha_{\text{sh}}(x) \Gamma_{\parallel e} (1 - n_{\text{floor}} / n), & x > x_{\text{sep}} \end{cases} \quad (\text{A21})$$

$$\nabla_{//} \Gamma_{\parallel i} = \begin{cases} 0, & x \leq x_{\text{sep}} \\ \alpha_{\text{sh}}(x) \Gamma_{\parallel i \text{SL}} (1 - n_{\text{floor}} / n), & x > x_{\text{sep}} \end{cases} \quad (\text{A22})$$

$$\nabla_{\parallel} Q_{\parallel e} = \left\{ \begin{array}{l} 3.21 \bar{T}_e \nabla_{\parallel} \Gamma_{\parallel e}, x \leq x_{\text{sep}} \\ \left(\nabla_{\parallel} q_{\parallel e} + \frac{5}{2} T_e \nabla_{\parallel} \Gamma_{\parallel e} - 0.71 T_e \nabla_{\parallel} j_{\parallel} \right) (1 - p_{e, \text{floor}} / p_e), x > x_{\text{sep}} \end{array} \right\} \quad (\text{A23})$$

$$\nabla_{\parallel} Q_{\parallel i} = \left\{ \begin{array}{l} 0, x \leq x_{\text{sep}} \\ \frac{5}{2} T_i \nabla_{\parallel} \Gamma_{\parallel i} (1 - p_{i, \text{floor}} / p_i), x > x_{\text{sep}} \end{array} \right\} \quad (\text{A24})$$

$$\nabla_{\parallel} j_{\parallel} = \left\{ \begin{array}{l} \alpha_{\text{dw}}(x) \bar{T}_e^{3/2} \{ \phi - T_e \ln(n) \}, x \leq x_{\text{sep}} \\ \alpha_{\text{sh}}(x) j_{\text{Padé}}, x > x_{\text{sep}} \end{array} \right\} \quad (\text{A25})$$

Appendix B Power balance

Power balance [viz., $P_{\text{SOL}} = P_{\text{div}} + P_{\text{loss}}$, in Eqs. (12)] is not ensured unless the ambiguity introduced by our ad hoc choice of the extent of the bi-normal (y) domain size, L_y , is rectified. If all of the turbulence were concentrated in a sub-domain smaller than L_y then this would not be an issue. However, the model uses periodic boundary conditions in y , and equilibria are statistically homogeneous in y . In reality, the turbulent flux is concentrated in a poloidal band ($\Delta\theta$) about the outboard midplane. So, we introduce an effective domain length, $L_{\theta} = a\Delta\theta$, and replace the y -integrals in Eqs. (12a) and (12c) with $L_{\theta} \langle f \rangle_y$, where f stands for either integrand, and “ a ” is the semi-minor radius of the machine. With this substitution, Eq. (12a) becomes

$$P_{\text{SOL}} = 2\pi R_m L_{\theta} \bar{Q}_{\perp} \Big|_{\Delta x=0} \quad (\text{B1})$$

where Q_{\perp} is the radial flux in the integrand of Eq. (12a).

To determine L_{θ} we exploit power balance in equilibrium and in the absence of dissipation and losses, viz., $\nabla_{\perp} Q_{\perp} = -\nabla_{\parallel} Q_{\parallel}$, which, after integrating over the SOL, y -averaging and applying the recipe $\nabla_{\parallel} \rightarrow 1/L_{\parallel}(x)$, becomes

$$\bar{Q}_{\perp} \Big|_{\Delta x=0} = \int_{\Delta x > 0} dx \bar{Q}_{\parallel} / L_{\parallel}(x). \quad (\text{B2})$$

(Q_{\perp} vanishes at the far-SOL boundary.) Using (B2) in (B1) and requiring $P_{\text{SOL}} = P_{\text{div}}$ yields

$$L_{\theta} = b_{\theta} \int_{\Delta x > 0} dx \bar{Q}_{\parallel} / \left[\int_{\Delta x > 0} dx \bar{Q}_{\parallel} / L_{\parallel}(x) \right] \equiv b_{\theta} \langle L_{\parallel}(x) \rangle_x. \quad (\text{B3})$$

In practice, we distinguish between electrons and ions and replace $\bar{Q}_{\parallel e, i}$ by their time-averages in equilibrium so that $L_{\theta e, i}$ are time-independent. For the three simulations we find $L_{\theta e, i} \cong (75, 72)$ cm and $\Delta\theta_{e, i} \equiv L_{\theta e, i} / a \cong 1.5$ rad for MAST-U ($a = 48.6$ cm). Since $L_{\theta} > L_y = 50$ cm, the simulation is properly contained within the effective turbulence domain, as befits a slice of reality.

References

- 1 A.O. Nelson, F.M. Laggner, R. Groebner, B.A. Grierson, O. Izacard, D. Eldon, M.W. Shafer, A. Leonard, D. Shiraki, A.C. Sontag, E. Kolemen and the DIII-D Team, "Setting the H-mode pedestal structure: variations of particle source location using gas puff and pellet fueling," *Nucl. Fusion* **60**, 046003 (2020), and references therein.
- 2 D.P. Stotler, J. Lang, C.S. Chang, R.M. Churchill and S. Ku, "Neutral recycling effects on ITG turbulence," *Nucl. Fusion* **57**, 086028 (2017).
- 3 T. D. Rognlien, D. D. Ryutov, N. Mattor and G. D. Porter, "Two-dimensional electric fields and drifts near the magnetic separatrix in divertor tokamaks," *Phys. Plasmas* **6**, 1851 (1999).
- 4 S. Wiesen, D. Reiter, V. Kotov, M. Baelmans, W. Dekeyser, A. S. Kukushkin, S. W. Lisgo, R. A. Pitts, V. Rozhansky, G. Saibene, I. Veselova and S. Voskoboynikov, "The new SOLPS-ITER code package," *JNM* **463**, 480 (2015).
- 5 X. Q. Xu, R. H. Cohen, T. D. Rognlien, and J. R. Myra, "Low-to-high confinement transition simulations in divertor geometry," *Phys. Plasmas* **7**, 1951 (2000).
- 6 F. Riva, F. Militello, S. Elmore, J. T. Omotani, B. Dudson, N. R. Walkden and the MAST team, "Three-dimensional plasma edge turbulence simulations of the Mega Ampere Spherical Tokamak and comparison with experimental measurements," *Plasma Phys. Control. Fusion* **61**, 095013 (2019).
- 7 S. I. Braginskii, "Transport processes in a plasma," *Rev. Plasma Phys.* **1** 205 (1965).
- 8 Z. H. Wang, X. Q. Xu, T. Y. Xia, and T. D. Rognlien, *Nucl. Fusion* **54**, 043019 (2014).
- 9 N. Bisai and P. K. Kaw, "Role of neutral gas in scrape-off layer of tokamak plasma in the presence of finite electron temperature and its gradient," *Phys. Plasmas* **23**, 092509 (2016).

-
- 10 N. Bisai and P. K. Kaw, “Influence of hot and cold neutrals on scrape-off layer tokamak plasma turbulence,” *Phys. Plasmas* **25**, 012503 (2018).
 - 11 N. Bisai, Santanu Banerjee, and Deepak Sangwan, “Modification of plasma flows in edge and SOL regions by influence of neutral gas,” *Phys. Plasmas* **25**, 102503 (2018).
 - 12 A. S. Thrysøe, M. Løiten, J. Madsen, V. Naulin, A. H. Nielsen, and J. Juul Rasmussen, “Plasma particle sources due to interactions with neutrals in a turbulent scrape-off layer of a toroidally confined plasma,” *Phys. Plasmas* **25**, 032307 (2018).
 - 13 A. S. Thrysøe, J. Madsen, V. Naulin, and J. Juul Rasmussen, “Influence of molecular dissociation on blob-induced atom density perturbations,” *Nucl. Fusion* **58**, 096005 (2018).
 - 14 C. Wersal and P. Ricci, “A first-principles self-consistent model of plasma turbulence and kinetic neutral dynamics in the tokamak scrape-off layer,” *Nucl. Fusion* **55**, 123014 (2015).
 - 15 C. Wersal and P. Ricci, “Impact of neutral density fluctuations on gas puff imaging diagnostics,” *Nucl. Fusion* **57**, 116018 (2017).
 - 16 D. A. Russell, J. R. Myra and D. P. Stotler, “A reduced model of neutral-plasma interactions in the edge and scrape-off-layer: verification comparisons with kinetic Monte Carlo simulations,” *Phys. Plasmas* **26**, 022304 (2019).
 - 17 Y. L. Zhou, Z. H. Wang, X. Q. Xu, H. D. Li, H. Feng, and W. G. Sun, “Comparisons between tokamak fueling of gas puffing and supersonic molecular beam injection in 2D simulations,” *Phys. Plasmas* **22**, 012503 (2015).
 - 18 F. Koechl et al. “Evaluation of fueling requirements for core density and divertor heat load control in non-stationary phases of the ITER DT 15 MA baseline scenario,” *Nucl. Fusion* **60** 066015 (2020).

-
- 19 A.R. Polevoi, A. Loarte, A.S. Kukushkin, H.D. Pacher, G.W. Pacher and F. Köchl, “Analysis of fueling requirements in ITER H-modes with SOLPS-EPED1 derived scalings,” *Nucl. Fusion* **57** 022014 (2017).
- 20 Shintato Koikea, Toshiki Takahashia, Naoki Mizuguchib, Osamu Mitarai, “Simulation study on a merging core fueling technique for an advanced fuel fusion spherical tokamak reactor,” *Fusion Engineering and Design* **136**, 111–115 (2018).
- 21 F. Scotti, D. P. Stotler, R. E. Bell, B. P. LeBlanc, S. A. Sabbagh, V. A. Soukhanovskii, M. V. Umansky and S. J. Zweben, “Outer midplane neutral density measurements and H-mode fueling studies in NSTX-U,” *Nucl. Fusion* **61**, 036002 (2021).
- 22 A.N. Simakov and P.J. Catto, “Drift-ordered fluid equations for field-aligned modes in low-collisional plasma with equilibrium pressure pedestals,” *Phys. Plasmas* **10**, 4744 (2003), and erratum: *Phys. Plasmas* **11**, 2326 (2004).
- 23 D. A. Russell, D. A. D'Ippolito, J. R. Myra, J. M. Canik, T. K. Gray, and S. J. Zweben, “Modeling the effect of lithium-induced pedestal profiles on scrape-off-layer turbulence and the heat flux width,” *Phys. Plasmas* **22**, 092311 (2015), and references therein.
- 24 D. Moulton, B. Lipschultz, J. Harrison, “Detachment onset in MAST-U according to SOLPS-ITER,” 44th EPS Conference on Plasma Physics, O5.129, <http://ocs.ciemat.es/EPS2017PAP/html/author.html>
- 25 D. P. Stotler, F. Scotti, R. E. Bell, A. Diallo, B. P. LeBlanc, M. Podestà, A. L. Roquemore, and P. W. Ross, “Midplane neutral density profiles in the National Spherical Torus Experiment,” *Phys. Plasmas* **22**, 082506 (2015).
- 26 S. T. Zalesak, “Fully multidimensional Flux-Corrected Transport algorithms for fluids,” *J. Comput. Phys.* **31**, 335–362 (1979); S. T. Zalesak, “The design of flux-corrected transport

-
- (FCT) algorithms for structured grids,” D. Kuzmin et al. (eds.), Flux-Corrected Transport, Scientific Computation, DOI 10.1007/978-94-007-4038-9_2, © Springer Science+Business Media Dordrecht 2012, pg. 23.
- 27 W. H. Press, S. A. Teukolsky, W. T. Vetterling and B. P. Flannery, *Numerical Recipes in Fortran 77: The Art of Scientific Computing*, 2nd Edition, Cambridge University Press (1999), pg. 847.
- 28 J. R. Angus and M. V. Umansky, “Modeling of large amplitude plasma blobs in three-dimensions,” *Phys. Plasmas* **21**, 012514 (2014).
- 29 A. Loarte, S. Bosch, A. Chankin, S. Clement, A. Herrmann, D. Hill, K. Itami, J. Lingertat, B. Lipschultz, K. McCormick, R. Monk, G. D. Porter, M. Shimada, and M. Sugihara, “Multi-machine scaling of the divertor peak heat flux and width for L-mode and H-mode discharges,” *J. Nucl. Mater.* **266–269**, 587–592 (1999).
- 30 A. J Thornton, A. Kirk and the MAST Team, "Scaling of the scrape-off layer width during inter-ELM H modes on MAST as measured by infrared thermography," *Plasma Phys. Control. Fusion* **56**, 055008 (2014).
- 31 J. R. Myra, D. A. Russell, D. A. D’Ippolito, J.-W. Ahn, R. Maingi, R. J. Maqueda, D. P. Lundberg, D. P. Stotler, S. J. Zweben, J. Boedo, M. Umansky, and NSTX Team, “Reduced model simulations of the scrape-off-layer heat-flux width and comparison with experiment,” *Phys. Plasmas* **18**, 012305 (2011).
- 32 D. A. D’Ippolito, J. R. Myra and S. J. Zweben, “Convective transport by intermittent blob-filaments: comparison of theory and experiment,” *Phys. Plasmas* **18**, 060501 (2011).

-
- 33 J. R. Myra, D. A. D’Ippolito, D. A. Russell, M. V. Umansky and D. A. Baver, “Analytical and numerical study of the transverse Kelvin–Helmholtz instability in tokamak edge plasmas,” *J. Plasma Phys.*, **82**, 905820210 (2016).
- 34 K. H. Burrell, “Effects of $\mathbf{E}\times\mathbf{B}$ velocity shear and magnetic shear on turbulence and transport in magnetic confinement devices,” *Phys. Plasmas* **4**, 1499–1518 (1997).
- 35 O. E. Garcia and A. Theodorsen, “Power law spectra and intermittent fluctuations due to uncorrelated Lorentzian pulses,” *Phys. Plasmas* **24**, 020704 (2017).
- 36 S.M. Kaye, R. Maingi, D. Battaglia, R.E. Bell, C.S. Chang, J. Hosea, H. Kugel, B.P. LeBlanc, H. Meyer, G.Y. Park and J.R. Wilson, “L-H threshold studies in NSTX,” *Nucl. Fusion* **51**, 113019 (2011).
- 37 P. C. Stangeby, *The Plasma Boundary of Magnetic Fusion Devices*, Institute of Physics Publishing, Bristol and Philadelphia, PA, 2000.
- 38 M. Wakatani and A. Hasegawa, *Phys. Fluids* **27**, 611 1984; A. Hasegawa and M. Wakatani, *Phys. Rev. Lett.* **59**, 1581 1987.

This report was prepared as an account of work sponsored by an agency of the United States Government. Neither the United States Government nor any agency thereof, nor any of their employees, makes any warranty, express or implied, or assumes any legal liability or responsibility for the accuracy, completeness, or usefulness of any information, apparatus, product, or process disclosed, or represents that its use would not infringe privately owned rights. Reference herein to any specific commercial product, process, or service by trade name, trademark, manufacturer, or otherwise does not necessarily constitute or imply its endorsement, recommendation, or favoring by the United States Government or any agency thereof. The views and opinions of authors expressed herein do not necessarily state or reflect those of the United States Government or any agency thereof.